



Doctoral Thesis in Physics

# Thermo-mechanical Assessment of Reactor Pressure Vessels of Light Water Reactors During Severe Accidents

HONGDI WANG

# Thermo-mechanical Assessment of Reactor Pressure Vessels of Light Water Reactors During Severe Accidents

HONGDI WANG

Academic Dissertation which, with due permission of the KTH Royal Institute of Technology, is submitted for public defence for the Degree of Doctor of Philosophy on Monday, the 16th October, 2023, at 10:00 a.m. in FA32, AlbaNova University Center, Stockholm.

Doctoral Thesis in Physics  
KTH Royal Institute of Technology  
Stockholm, Sweden 2023

© Hongdi Wang

ISBN 978-91-8040-703-8

TRITA-SCI-FOU 2023:42

Printed by: Universitetservice US-AB, Sweden 2023

*To my husband*

*Xiaolei*



## **Abstract**

The reactor pressure vessel (RPV) is one of the crucial safety barriers designed to isolate the reactor core, safeguarding against potential radioactive releases into the environment during a severe accident. The assessment of RPV behaviour and its failure is necessary to predict the characteristics of melt release into the reactor pit and succeeding ex-vessel accident progression.

This thesis aims to develop both the model and methodology in the Finite Element Analysis (FEA) of the RPV to predict its structural behaviour during postulated severe accidents. The improvement in the FE model starts from the material models for the material properties of the RPVs. Since the SA533B1 and 16MND5 carbon steels are considered the structural materials of the RPVs relevant to a Nordic Boiling Water Reactor (BWR) and a Pressurized Water Reactor (PWR), respectively, the material models for these two materials are established and subsequently validated against multiple tests. The simulations strictly adhere to the test conditions in the validation process. The observed agreement between the simulation and test results serves as a good foundation for subsequent analysis on the RPV applications.

A thermo-mechanical coupling approach is developed by coupling the ANSYS Mechanical APDL for the structural analysis of RPVs and MELCOR for defining boundary conditions. This approach can efficiently predict the RPV behaviour during accident scenarios, including deformation, stress and strain. Subsequently, the obtained results are subjected to a comprehensive failure analysis of RPVs with three failure criteria, namely melt-through, stress-based, and strain-based failure criteria. In addition, an advanced model in LS-DYNA is introduced to simulate the possible rupture phenomenon of RPVs during failure.

The developed model and methodology are applied in structural analysis of the Nordic BWR and the PWR during severe accidents. The analysis results contribute to:

- (i) A benchmark specification in the EU-IVMR project WP2.4 conducted to investigate the effect of the ablated profile on RPV failure in numerical analysis;
- (ii) The feasibility of In-Vessel Retention (IVR) strategy mitigation analyzed for the RPV of a Nordic BWR in two severe accidents: a Station Blackout (SBO) and an SBO combined with a Loss-of-coolant Accident (SBO+LOCA); and

- (iii) A comprehensive failure analysis for RPVs in a Nordic BWR carried out under the mentioned two severe accidents. The RPV lower plenum model is extended from the two-dimensional case for a standalone vessel wall to a three-dimensional case for a vessel wall with a cluster of IGT structures. This failure analysis aims to investigate the failure mechanism and timing for both vessel wall and IGTs, providing valuable insights into the possible earliest failure mode of RPV lower plenum for different reactor designs and severe accident scenarios.

**Keywords:** Severe accident scenario, reactor pressure vessel, in-vessel melt retention, failure analysis, finite element analysis, validations

## Sammanfattning

Reaktortanken utgör en central säkerhetskomponent som är utformad för att fungera som en barriär för att isolera och skydda reaktorhärden i händelse av ett allvarligt haveri, med syftet att förhindra eventuella radioaktiva utsläpp till miljön. För att förebygga och förutsäga händelseförloppet vid ett sådant scenario, krävs en grundlig bedömning av reaktortankens beteende och eventuella brott i dess struktur.

I denna avhandling har en modell och en metodik utvecklats i Finite Element Analyser (FEA) för att förbättra förståelsen av reaktortankens strukturella beteende under postulerade svåra haverier. Förbättringen av den använda modellen fokuserar på att korrekt beskriva materialegenskaperna hos de två relevanta reaktortankstålarna för de nordiska kokar – respektive tryckvattenreaktorer, SA533B1 och 16MND5. Denna konstitutiva modell har blivit noggrant validerad genom att jämföra dess resultat med flera experimentella tester, och överensstämmelsen mellan simuleringar och tester har styrkt dess tillförlitlighet.

För att kunna förutsäga reaktortankens beteende under olika svåra haveriscenarier, inklusive deformation, stress och belastning, har en termo-mekanisk kopplingsmetod utvecklats. Denna metod kopplar ANSYS Mechanical APDL för strukturanalys av reaktortanken med MELCOR för att definiera de nödvändiga randvillkoren. Resultaten av dessa analyser har använts för att genomföra en omfattande felanalys av reaktortanken med hjälp av tre olika brottkriterier: genomsmältning, spänningsbaserat och töjningsbaserat brottkriterium. Dessutom har en avancerad modell i LS-DYNA använts för att simulera brottfenomenet i reaktortanken under haverier.

Denna simuleringsmodell och metodik har tillämpats på reaktortanksapplikationer för både nordiska kokvattenreaktorer (BWR) och tryckvattenreaktorer (PWR). Resultaten av analyserna har bidragit till:

- (i) En benchmarkstudie inom EU-IVMR-projektet WP2.4 för att utvärdera effekterna av en eventuell borttagning av reaktortankens profil i numeriska analyser;
- (ii) Analyser av genomförbarheten av in-vessel retention (IVR), en strategi för haverihantering som innebär att härdsmltan stannar kvar i reaktortanken och kyles utifrån. Denna strategi har utvärderats för en nordisk BWR under

två olika svåra haveriscenarier: totalt elbortfall (SBO) och en kombination av SBO och kylmedelshaveri (SBO+LOCA); och

- (iii) En djupgående felanalys av reaktortanken i en nordisk BWR under de två nämnda svåra haveriscenarierna. Modellen för reaktortankens botten har modifierats från att vara tvådimensionell till att vara tredimensionell med ett kluster av instrumentgenomföringar. Denna felanalys syftar till att utforska brottmekanismer och tidpunkter för brott, både för reaktortanken och instrumentgenomföringarna, och ger värdefulla insikter om tidiga brottmekanismer i reaktortankens botten för olika reaktorkonstruktioner och svåra haveriscenarier.

**Nyckelord:** Scenario för svåra haverier, reaktortank, in-vessel retention, feleffektsanalys, Finite Element Analyser, validering

## List of Publications

### Publications included in this thesis

**Paper 1.** Wang, H.D., Villanueva, W., Structural behaviour of an ablated reactor pressure vessel wall with external cooling, *Progress in Nuclear Energy*, 153 (2022) 104446.

**Paper 2.** Wang, H.D., Villanueva, W., Chen, Y.L., Kulachenko, A., and Bechta, S., Thermo-mechanical behaviour of an ablated reactor pressure vessel wall in a Nordic BWR under in-vessel core melt retention, *Nuclear Engineering and Design*, 379 (2021) 111196.

**Paper 3.** Wang, H.D., Chen, Y.L., Villanueva, W., Vessel failure analysis of a boiling water reactor during a severe accident, *Frontiers in Energy Research*, 10 (2022) 839667.

**Paper 4.** Wang, H.D., Villanueva, W., Thermo-mechanical failure of a reactor vessel with penetrations during a severe accident, *Progress in Nuclear Energy*, under review.

### Author's contribution to the included publications

Hongdi Wang made major contributions to these four included publications under the guidance of supervisors and with the collaboration of other co-authors. Her contributions mainly focus on methodology development, data collection, code implementation, calculation, draft writing, and finalization of the paper in discussion with co-authors and reviewers.

### Publications not included in this thesis

**Paper 5.** Wang, H.D., Villanueva, W., and Chen, Y.L., Structural Failure of an Ablated Reactor Pressure Vessel Wall in Nordic-type BWR under a Severe Accident., 19th International Topical Meeting on Nuclear Reactor Thermal Hydraulics, (2022).

**Paper 6.** Hossny, K., Villanueva, W., Wang, H.D., Distinctive physical insights driven from machine learning modelling of nuclear power plant severe accident scenario propagation, *Scientific Reports*, 13 (2023) 930.

**Paper 7.** Yue, Y., Villanueva, W., Wang, H.D., and Wang, D., Thermo-Mechanical Analysis of Instrumentation Guide Tube Failure During a Severe Accident in a Nordic

Boiling Water Reactor., the International Conference on Nuclear Engineering (ICONE) 2020. American Society of Mechanical Engineers, (2020).

**Paper 8.** Villanueva, W., Filippov, A., Jules, S.; Lim, K.; Jobst, M., Bouydo, A.M., Qais, S., Wang, H.D., Fichot, F., Bechta, S., Thermo-mechanical modelling of reactor pressure vessel during core melt in-vessel retention, Proc. of the International Seminar on In-vessel retention: outcomes of the IVMR project, Juan-les-Pins, France, (2020).

## **Acknowledgement**

First and foremost, I would like to express my deepest gratitude to my main supervisor Prof. Walter Villanueva, for your invaluable support, mentorship, encouragement, and patience throughout my doctoral study. I am truly fortunate to have studied under your supervision, and immensely grateful for the immeasurable impact you have had on my academic and personal growth.

I would like to thank my co-supervisors Prof. Sevostian Bechta and Prof. Weimin Ma, for offering the valuable opportunity to study at KTH, and also for all the support and discussions. With your help, I learnt a lot about nuclear engineering. I am also thankful to my co-supervisor Prof. Artem Kulachenko, who offers me insightful comments and inspiring ideas about mechanical engineering.

Thank you so much to Prof. Jan Dufek for reviewing the draft of the thesis and thank you to Mr. Sean Roshan Ghias for the help with the Swedish Abstract.

I am grateful to all my colleagues at Division of Nuclear Power Safety. Your support and company have made this PhD journey more enjoyable and more meaningful. A deep thank goes to Yan Xiang and Yangli, for your willingness to share knowledge and offer a helping hand every moment.

Special thanks to all my friends. Thank you Yangli, Lu Zhao and Ying Xu, for always being there to lend a listening ear and offer a shoulder to lean through the ups and downs, the laughter, and tears.

I would like to express my heartfelt gratitude to my parents, brothers, and sisters. Thank you for your unconditional love and understanding, and it has made me feel cherished and valued as a member of this wonderful family.

Last and most importantly, I would like to express my deepest gratitude and appreciation to my beloved husband, Xiaolei, for the warmth, hope, and happiness you bring into my life. Your strength, resilience, and determination motivate me to face life's challenges with confidence and grace. With you by my side, I know that we can overcome any challenges. Thank you for making me smile and laugh every day, actually not every day, but almost every day during the past nine years. Thank you for being an incredible husband, and I am forever grateful to have you in my life.



## Contents

<b>Abstract.....</b>	<b>i</b>	
<b>Sammanfattning .....</b>	<b>iii</b>	
<b>List of Publications...</b>	<b>v</b>	
<b>Acknowledgement ....</b>	<b>vii</b>	
<b>Contents .....</b>	<b>ix</b>	
<b>Nomenclature.....</b>	<b>xi</b>	
<b>Chapter 1 .....</b>	<b>Introduction .....</b>	<b>1</b>
1.1	Background .....	1
1.2	Objectives and contributions.....	4
1.3	Thesis outline .....	4
<b>Chapter 2 .....</b>	<b>Material Models and failure mechanism .....</b>	<b>7</b>
2.1	Basis of continuum mechanics.....	7
2.1.1	Stress and strain.....	7
2.1.2	Creep and models .....	10
2.1.3	Elastoplasticity and models .....	11
2.2	Modelling of RPV steels and validations .....	13
2.2.1	16MND5 carbon steel .....	14
2.2.2	SA533B1 carbon steel.....	17
2.3	Failure mechanisms .....	18
2.3.1	Melt-through.....	19
2.3.2	Stress failure.....	19
2.3.3	Strain failure.....	20
<b>Chapter 3 .....</b>	<b>Computational framework and tools.....</b>	<b>21</b>
3.1	Computational framework .....	21
3.2	MELCOR.....	23
3.3	ANSYS Mechanical APDL .....	23

3.4	LS-DYNA .....	25
<b>Chapter 4</b>	<b>Application to structural analysis in PWR design.....</b>	<b>33</b>
4.1	Benchmark problem .....	33
4.2	FE model .....	34
4.3	Results and discussion.....	36
<b>Chapter 5</b>	<b>Application to structural analysis in BWR design .....</b>	<b>39</b>
5.1	IVR feasibility .....	39
5.1.1	MELCOR model.....	39
5.1.2	FE model.....	41
5.1.3	Results and discussion .....	42
5.2	RPV failure analysis.....	45
5.2.1	MELCOR model.....	46
5.2.2	FE model.....	46
5.2.3	Results and discussion .....	47
5.3	Penetration failure analysis .....	51
5.3.1	FE model.....	53
5.3.2	Results and discussion .....	53
<b>Chapter 6</b>	<b>Conclusions and outlook .....</b>	<b>57</b>
6.1	Conclusions .....	57
6.2	Outlook.....	58
<b>References</b>	<b>.....</b>	<b>59</b>

# Nomenclature

## Acronyms

ADS	Automatic Depressurization System
APDL	Ansys Parametric Design Language
BWR	Boiling Water Reactor
CAV	Cavity Package
CEA	French Alternative Energies and Atomic Energy Commission
CHF <sub>s</sub>	Critical Heat Fluxes
COR	Core Package
CTH	Combined time hardening
CRGT	Control Rod Guide Tube
DCH	Decay Heat Package
ERV <sub>C</sub>	External Reactor Vessel Cooling
FEA	Finite Element Analysis
FEM	Finite Element Model
FIP	Failure Internal Pressure
FT	Failure Time
HPC	High Performance Computing
IGT	Instrumentation Guide Tube
INEL	Idaho National Engineering Laboratory
IVR	In-vessel Melt Retention
LHF	Lower Head Failure
LOCA	Loss-of-coolant Accident
NB	Norton-Bailey
NISO	Nonlinear Isotropic

NPP	Nuclear Power Plant
OLHF	OECD Lower Head Failure
PWR	Pressurized Water Reactor
RAM	Random Access Memory
RCIC	Reactor Core Isolation Cooling
RMSE	Root Mean Square Error
RPV	Reactor Pressure Vessel
RT14	RUPATHER Test #14
SAM	Severe Accident Management
SBO	Station Blackout
SDG	Sustainable Development Goals
SH	Strain hardening
TMI-2	Three Mile Island Unit 2

## Latin symbols

$A$	cross-sectional area
$b$	material constant
$C$	damping matrix
$c$	a matrix of material constants
$c_i$	constants
$D$	displacement vector
$E$	Young's module
$F$	external force
$F_b$	vector of the body force on a node
$F_S$	vector of the surface force on a node
$f_e$	total nodal force vector

$f_b$	vector of the body force on an element
$f_s$	vector of surface force on an element
$G$	shear modulus
$K$	global stiffness matrix
$k_e$	element stiffness matrix
$L$	original length
$\Delta L$	the change of length
$M$	global mass matrix
$m_e$	element mass matrix
$R_0$	material constant
$R_\infty$	material constant
$S$	the surface of a solid
$T$	temperature
$T$	kinetic energy
$V$	the whole volume of a solid
$\nu$	Poisson's ratio
$W_f$	work
$x$	force direction

### Greek symbols

$\varepsilon$	strain scalar
$\boldsymbol{\varepsilon}$	tensor of strain
$\varepsilon_{Total}$	total strain
$\varepsilon_{creep}$	creep strain
$\varepsilon_{plastic}$	plastic strain

$\varepsilon_{elastic}$	elastic strain
$\xi^{pl}$	accumulated equivalent plastic strain
$\varepsilon_0$	initial instantaneous strain
$\dot{\varepsilon}_{cr}$	creep strain rate
$\sigma$	stress scalar
$\boldsymbol{\sigma}$	tensor of stress
$\sigma_0$	initial yield stress
$\delta_Y$	current yield stress
$\Pi$	potential energy

# Chapter 1 Introduction

## Introduction

### 1.1 Background

Nuclear energy, a clean and reliable energy source, provides over 370 GWe of electricity for both industrial manufacturing and household consumption, utilizing more than 400 nuclear reactors globally. The growth of nuclear energy has made a significant impact on the increase of low-carbon electricity worldwide, thus contributing to the global Sustainable Development Goals (SDGs) [1]. To isolate fission products from the public domain, general Nuclear Power Plants (NPPs) incorporate three critical physical barriers: the fuel cladding, the reactor pressure vessel (RPV), and the containment. As the second safety barrier, the RPV, which encloses the reactor core, plays a critical role in determining the life limit of an NPP. More importantly, the behaviour of the RPVs strongly affects the progression and consequences of any potential nuclear accident. This thesis is believed to be close to the safety and advancement of nuclear power by contributing to the investigation of RPV integrity during postulated reactor accidents.

Two types of reactor accidents have been extensively studied and analyzed in the field of nuclear power safety: the station blackout (SBO) scenario and the Loss-of-coolant (LOCA) scenario. SBO accidents describe an event characterized by the loss of electrical power. It is not uncommon, but the Fukushima disaster is still the most famous. In the Fukushima nuclear accident that occurred in 2011, a strong earthquake and a subsequent tsunami lead to the loss of electrical power at three operating units (unit 1,2, and 3), disabling multiple cooling systems and inducing significant damage to the reactor buildings [2-6]. On the other hand, LOCA accidents describe an event in which coolant is lost from the reactor core. A famous event of this scenario is the Three Miles Island accident in 1979, where the loss of coolant affects the heat removal safety function [7-10]. These two types of scenarios can occur independently or in combination [11-13].

In SBO and LOCA scenarios, the reactor core is vulnerable to overheating, potentially leading to core meltdown accidents. During such events, the original core configuration, including fuel rods and structural composition, is subjected to extreme heat and can melt due to the termination of the reactor core isolation cooling (RCIC). This results in the formation

of a debris bed that relocated to the lower head of the RPVs. This debris bed imposes a continuous thermo-mechanical load on the RPV, posing a significant threat to its structure integrity. If the RPV fails, according to the current understanding, highly superheated corium melt will be released into the water pool. The failure location and time of the RPV can dictate the ex-vessel accident progression (e.g., Fuel-coolant Interaction, Molten Core-Concrete Interaction, and possible energetic steam explosion as shown in Fig. 1.1) and further accident progression (e.g., the final damage state of the reactor and plant decommissioning efforts including debris removal and reprocessing).

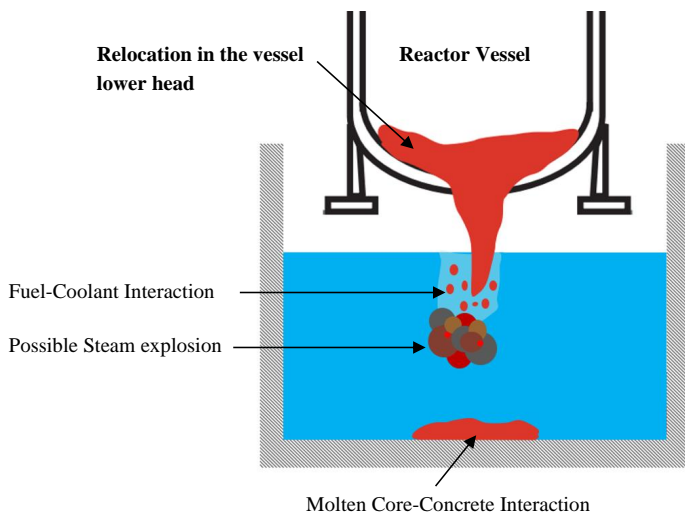


Figure 1.1. Scheme of the main ex-vessel events that can occur during a severe accident.

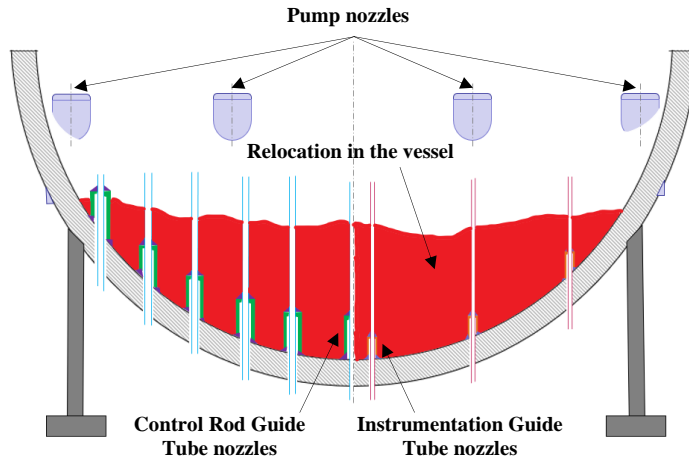


Figure 1.2. The layout of the RPV lower plenum in a Nordic BWR with melt relocation inside, including the structures of CRGTs, IGTs, and Pump nozzles.

Fig. 1.2 shows the configuration of the lower plenum of a Nordic BWR, incorporating the global vessel wall and internal penetrations (i.e., Instrumentation Guide Tubes, Control Rod Guide Tubes, and Pump Nozzles). The structural integrity of the vessel lower plenum may be lost due to the failure of global vessel wall or internal penetrations [14-16]. These failures can be assessed by investigating their thermo-mechanical behavior within the FE analysis.

Mitigation strategies aim to stabilize the molten corium and minimize the risks of containment failure during a severe accident. In-vessel melt retention (IVR) strategy is one of the attractive options and has been studied in recent years. The success of this strategy relies on removing the decay heat of the corium via water cooling outside the pressure vessel. The main factors that affect the effectiveness of the IVR strategy are (i) the heat flux from the corium to the RPV and (ii) the external cooling capability. The feasibility of this strategy can be investigated through safety analyses, including accurate prediction of vessel thermo-mechanical behaviour.

## 1.2 Objectives and contributions

A reliable modelling and an efficient methodology are critical for predicting the mode and timing of vessel failure during severe accident scenarios. Although it's widely explored, many research gaps remain. In this regard, the major contributions of this thesis can be summarized as follow:

- This study proposes and validates material models for two types of RPV structural materials, namely SA533B1 carbon steel used in BWR design and 16MND5 carbon steel used in PWR design. These models incorporate both elastoplasticity and creep models. With these material models, it becomes possible to predict macro-structural global deformation, and micro-structural stress-strain responses of the vessel walls under thermo-mechanical loads.
- This study establishes a unified framework with ANSYS and MELCOR platforms to predict the behaviour of an RPV lower head under severe accidents. This framework incorporates a one-way coupling method and considers the dynamic ablation of the vessel wall, and the effect of the ablated profile.
- This framework is employed in the failure analysis of an RPV within a Nordic BWR. The model of RPV lower plenum is extended from a two-dimensional case of a standalone vessel wall to a three-dimensional case of a vessel wall with a cluster of IGT structures. The goal of this failure analysis is to explore the failure mechanisms and timing for both the vessel wall and IGTs, thereby offering insights into the possible earliest failure mode of RPV lower plenum.
- The feasibility of IVR strategy is analyzed, considering the BWR design in two severe accident scenarios: (i) Station Blackout (SBO) and (ii) Station Black-out combined with Loss-of-coolant Accident (SBO+LOCA).

## 1.3 Thesis outline

This thesis includes six chapters. Chapter 2 demonstrates the fundamentals of continuum mechanics and presents model validations. Chapter 3 provides an overview of the MELCOR, ANSYS Mechanical APDL, and LS-DYNA platforms, along with the introduction of a unified framework for thermo-mechanical analysis of RPVs lower plenum. Chapter 4 presents a structural analysis of the RPV in a generic PWR1000 design. In Chapter 5, more attention is paid to the structural analysis of the RPV in a Nordic BWR during severe accident scenarios, including the vessel wall failure analysis, penetration failure analysis, and the

feasibility of the IVR strategy. Finally, the overall conclusions and future work are summarized in Chapter 6.



## Chapter 2 Material Models and failure mechanism

During a meltdown event, the RPVs are subjected to continuous thermo-mechanical loads from the molten corium, inducing sustained stress and strain on the structures of the RPV. This chapter introduces key concepts such as stress and strain, as well as their relationship, the relationships between stress and force, and strain and displacement. These relationships are vital in structural modelling and are reliant on material properties. Given that the vessel walls are forged from 16MND5 and SA533B1 carbon steel in PWR and BWR, respectively, this thesis includes and validates the material models for these two materials. The content of this chapter is mainly from papers 1 and 2.

### 2.1 Basis of continuum mechanics

#### 2.1.1 Stress and strain

The structures of the lower plenum of RPVs, including the vessel wall and the penetrations, are composed of solid materials. These structures are subjected to stress when external forces are applied. For initial understanding, we consider a one-dimensional solid as shown in Fig 2.1, where the external force  $F$  is applied solely in  $x$  direction. Stress is a quantity that describes the distribution of internal forces within a body, and strain is a dimensionless quantity resulting from the applied stress. The equations representing stress and strain are as follows:

$$\sigma = \frac{F}{A} \quad (2.1)$$

$$\varepsilon = \frac{\Delta L}{L} \quad (2.2)$$

where  $\sigma$  is the stress,  $F$  is the external force,  $A$  is the cross-sectional area,  $\varepsilon$  is the strain,  $L$  is the original length, and  $\Delta L$  is the change of length.

Depending on the inherent properties of a given material, solids can exhibit elastic, plastic, viscoplastic, or viscoelastic characteristics. These properties give different relationships between stress and strain, thereby necessitating different constitutive models. One fundamental relationship between stress and strain for a one-dimensional solid is provided by Hooke's law:

$$\sigma = E\epsilon \quad (2.3)$$

where Young's modulus  $E$  is the material constant, which can be obtained from a tensile test of the material.

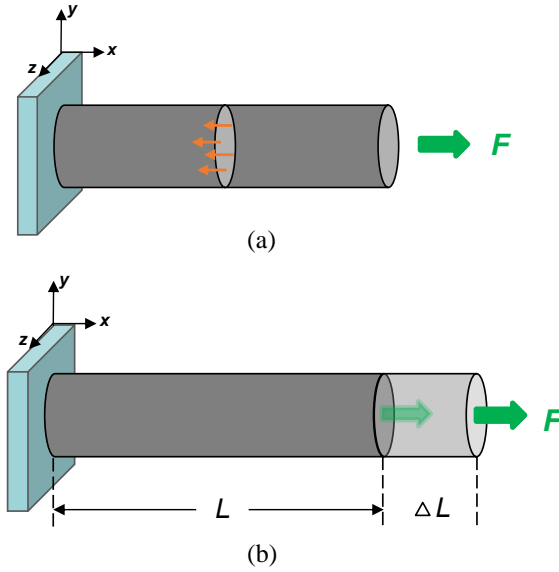


Figure 2.1. Illustration of a one-dimensional solid subjected to an external force along the x-axis.

At any point of 3D solids, indicated as an infinite small cube (see Fig. 2.2), the stress consists of the normal and shear stress components. Considering the shear equivalence relations ( $\sigma_{xy} = \sigma_{yx}, \sigma_{xz} = \sigma_{zx}, \sigma_{yz} = \sigma_{zy}$ ), the stress in 3D solids can be expressed by six independent stress components as Eq. (2.4). A similar vector form of the strain in 3D solids can be written as Eq. (2.5).

$$\boldsymbol{\sigma}^T = \{ \sigma_{xx} \ \sigma_{yy} \ \sigma_{zz} \ \sigma_{yz} \ \sigma_{xz} \ \sigma_{xy} \} \quad (2.4)$$

$$\boldsymbol{\varepsilon}^T = \{\varepsilon_{xx} \ \varepsilon_{yy} \ \varepsilon_{zz} \ \varepsilon_{yz} \ \varepsilon_{xz} \ \varepsilon_{xy}\} \quad (2.5)$$

Hence, Hooke's law can be written in a matrix form:

$$\boldsymbol{\sigma} = \begin{bmatrix} c_{11} & c_{12} & c_{13} & c_{14} & c_{15} & c_{16} \\ & c_{22} & c_{23} & c_{24} & c_{25} & c_{26} \\ & & c_{33} & c_{34} & c_{35} & c_{36} \\ & & & c_{44} & c_{45} & c_{46} \\ & sy. & & & c_{55} & c_{56} \\ & & & & & c_{66} \end{bmatrix} \boldsymbol{\varepsilon} = \mathbf{c}\boldsymbol{\varepsilon} \quad (2.6)$$

where  $\mathbf{c}$  is a matrix of material constants obtained from experiments.

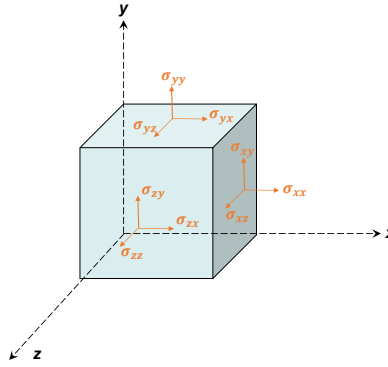


Figure 2.2. Stress components at a point of a 3D solid problem.

The behaviour of stress-strain, particularly RPV structures subjected to quite high temperatures, presents a complex phenomenon. In this condition, strain can be specifically decomposed into elastic, plastic, and creep strains. The elastic and plastic strains are time-independent; the former is characterized by total reversibility, while the latter by irreversibility when the applied stress is removed. In contrast, creep strain refers to slow, time-dependent deformation at elevated temperatures, typically occurring at 0.3-0.4 of the melting temperatures for RPV carbon steels [17, 18]. Thus, the total strain, denoted as  $\varepsilon_{Total}$ , can be expressed as the sum of creep  $\varepsilon_{creep}$ , plastic  $\varepsilon_{plastic}$ , and elastic  $\varepsilon_{elastic}$  as listed in Eq. (2.7). Worth note, in applications encountering high thermal loads, creep deformation is expected to play a dominate role[15, 19].

$$\varepsilon_{Total} = \varepsilon_{creep} + \varepsilon_{plastic} + \varepsilon_{elastic} \quad (2.7)$$

This thesis uses separate models for elastoplasticity and creep to describe the stress-strain behaviour of materials. This approach agrees with the studies in the literature [14, 20]. The selection of appropriate models depends on various factors, including the type of material, the availability of experimental data for materials, loading conditions, and the numerical tools. The models governing creep and elastoplasticity will be introduced in Section 2.1.2 and Section 2.1.3, respectively.

### 2.1.2 Creep and models

Creep behaviour is closely affected by both the applied stress and temperature. Controlling these two factors, Fig. 2.3 shows the typical stages of creep behaviour under a constant stress  $\sigma_1$  and temperature  $T_1$ , namely, the primary, secondary, and tertiary stages. The deformation rate during this process is referred the ‘creep rate’. During the primary stage, the creep rate gradually decreases until it stabilizes at a certain value in the second phase, which is termed the ‘steady-state creep’. Subsequently, in the tertiary stage, the creep rate increases rapidly until it culminates in a creep rupture. Generally, a higher stress  $\sigma_2$  or temperature  $T_2$  will lead to a shorter secondary stage and a shorter time to rupture [21, 22]. As per the REVISIA-experiments, the creep curve for RPV carbon steels typically initiates the secondary and tertiary stages around 0.1 and 0.2 creep strains, respectively, and ruptures below 0.6 creep strain for any given stress and temperature conditions [23, 24].

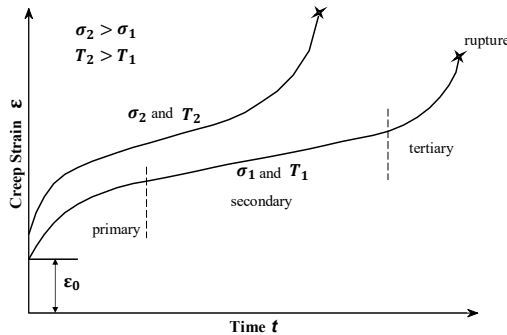


Figure 2.3. Typical creep curve showing the three stages ( $\varepsilon_0$ =initial instantaneous strain).

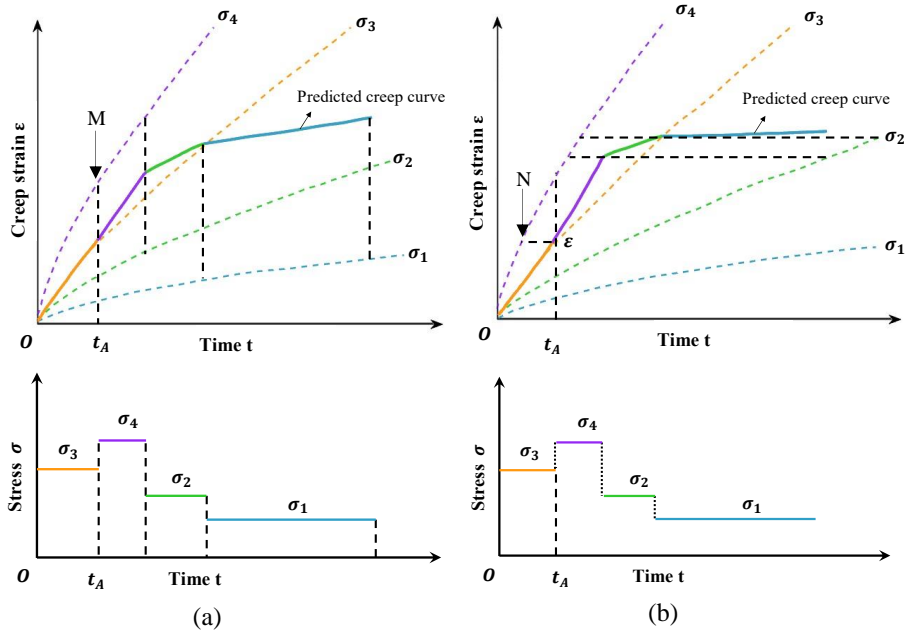


Figure 2.4. (a) creep evolution of time hardening creep model. (b) creep evolution of strain hardening creep model.

For thermo-mechanical analysis in mechanical tools, time hardening and strain hardening creep models are most employed to describe creep behaviour. Fig. 2.4 illustrates four dotted lines, each predicting creep behaviour under four distinct applied stresses ( $\sigma_1$ ,  $\sigma_2$ ,  $\sigma_3$ , and  $\sigma_4$ ). For instance, when the applied stress shifts from  $\sigma_3$  to  $\sigma_4$  at time  $t_A$ , the time hardening creep model adjusts its predictive curve to follow the creep trajectory under  $\sigma_4$  from the point at the current time  $t_A$  (marked as ‘M’ in Fig. 2.4 (a)). By comparison, the strain hardening creep model traces the creep curve under  $\sigma_4$  from the point at the current creep strain  $\epsilon$  (marked as ‘N’ in Fig. 2.4 (b)).

### 2.1.3 Elastoplasticity and models

Material behaviour is assumed to be composed of the creep behaviour and the elastoplastic behaviour, representing a complex behaviour when combined. This section will introduce the elastoplastic response of materials.

The elastoplastic response of materials is described as a mathematical relationship by three plasticity theories: the flow rule, yield criterion, and hardening rule. The key characteristics of these three theories can be demonstrated in a one-dimensional mathematical model. Refer to Fig. 2.5, presenting the mathematical stress-strain curves for a ductile metal subjected to a uniaxial tension test.

The elastic and plastic regions in the model are delimited by the yield stress, denoted by  $\sigma_0$ . When the material experiences a load ranging from zero to  $\sigma_1$  ( $\sigma_1 < \text{initial yield stress } \sigma_0$ ), the behaviour of the material behaviour can be considered perfectly reversible (i.e., elastic behaviour). That is, the unloading trajectory  $AO$  retraces the loading path  $OA$ , returning to the original state.

However, when the material is subjected to a load ranging from zero to a higher stress  $\sigma_2$  ( $\sigma_2 > \sigma_0$ ), it experiences irreversible deformation. Under such loading condition, the material will return to Point  $O_1$  following path  $BO_1$  when the load is released. The new unstressed point  $O_1$  diverges from the original unstressed point  $O$ , marking a permanent deformation strain  $\epsilon_p$  for the material. This permanent strain contributes to the yield strength  $CB$ , inducing a new yield strength point  $B$ . This change within the material is called strain hardening [25]. Furthermore, when conceptualizing plastic strain as a vector, the sign of the increment in plastic strain is the same as that in stress. This is also known as the flow rule.

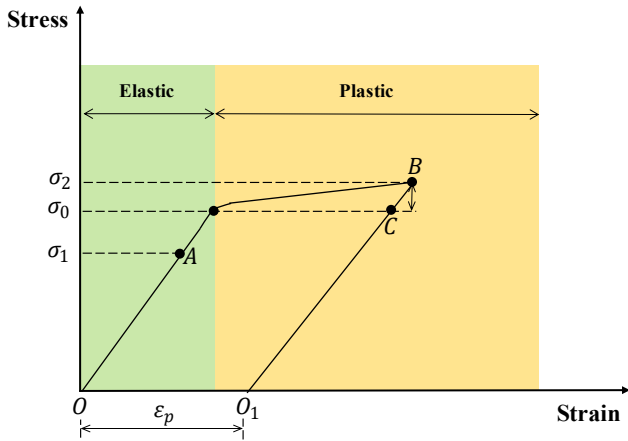


Figure 2.5. Uniaxial tension experiment with ductile metals.

The concept of the initial yield stress point can be extended to the yield surfaces in 2D plasticity and 3D plasticity, as illustrated in Fig. 2.6. Based on the three plasticity theories, more complex constitutive models are developed to describe the elastoplastic behaviour of materials.

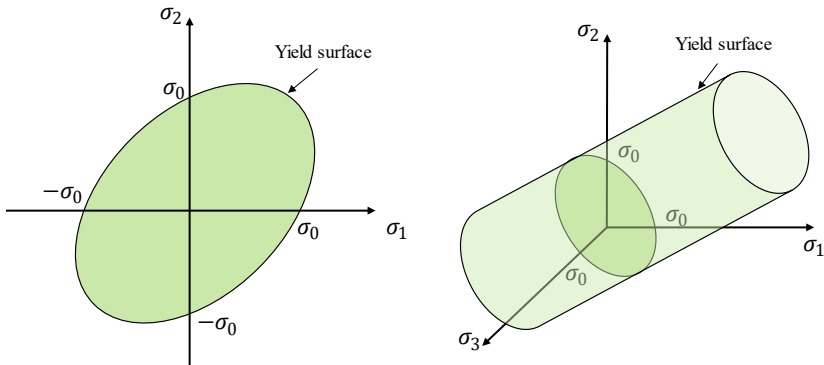


Figure 2.6. Von Mises yield surfaces in 2D and 3D conditions.

## 2.2 Modelling of RPV steels and validations

The RPVs undergo harsh conditions, especially during severe accidents. The properties of the structural material used in the RPVs are vital to meet the requirements of safety and economy of a nuclear power plant [26-28]. Low-alloy steel is the material commonly used in RPVs structures, such as US SA533B1, French 16MND5, and Russian 15Kh2NMFAA. These materials have exceptional strength, toughness and weldability [29-30].

Table 2.1. Chemical composition of the SA533B1 and 16MND5.

Material	C	Si	Mn	P	S	Ni	Cr	Mo	V	Cu	A	Co	Nb	B	H
SA533B1	170	250	1440	4	2	750	200	510	4	10	1	4	1	0.1	0.9
16MND5	170	200	1220	6	10	670	100	550	3	9	-	-	-	-	-

In the scope of this thesis, the focus will be on US SA533B1 and French 16MND5, which are used as the structural materials of the RPVs within Nordic BWRs and PWRs, respectively. The chemical compositions of these materials are summarized in Table 2.1. Subsequently, the material models and validations for these two RPV materials will be presented. The material data includes ultimate strength, specific heat capacity, density,

thermal conductivity, coefficient of thermal expansion, and Young's modulus. Notably, each of these properties is a function of temperature.

### 2.2.1 16MND5 carbon steel

For the material properties of 16MND5, available data from [15] is adopted. Two key models have been established: a nonlinear isotropic (NISO) hardening model, as in Eq. (2.8), used for investigating elastoplasticity, and a strain hardening model as in Eq. (2.9), used for investigating creep.

$$\delta_Y = \sigma_0 + R_0 \varepsilon^{pl} + R_\infty (1 - \exp(-b \varepsilon^{pl})) \quad (2.8)$$

where  $\delta_Y$  is the current yield stress,  $\sigma_0$  is the initial yield stress,  $\varepsilon^{pl}$  is the accumulated equivalent plastic strain, and  $R_\infty$ ,  $R_0$ , and  $b$  are material constants.

$$\dot{\varepsilon}_{cr} = c_1 \delta \varepsilon_{cr}^{c_2} \varepsilon_{cr}^{c_3} e^{c_4/T} \quad c_1 > 0 \quad (2.9)$$

where  $\dot{\varepsilon}_{cr}$  is the creep strain rate in units of 1/s,  $T$  is the temperature,  $\sigma$  is the stress and  $c_1 \sim c_4$  are the constant parameters.

Table 2.2. Parameters of NISO hardening model at different temperatures for 16MND5.

T	473K	673K	873K	973K	1273K	1373K	1473K	1573K
$\sigma_0$	4.13E8	3.76E8	3.00E8	1.31E8	3.03E7	1.64E7	1.04E7	4.66E6
$R_0$	-1.3E10	-7.2E9	-3.4E9	-3.7E8	-2.2E8	-4.8E7	-1.2E7	-1.5E7
$R_\infty$	4.91E9	1.70E9	1.16E9	1.08E8	1.42E8	1.52E7	2.70E6	5.58E6
$b$	3.83	8.18	3.98	3.01	2.44	16.17	76.09	18.51

Table 2.3. Parameters of strain hardening model at different temperatures for 16MND5.

T	643K	873K	1173K	1273K	1373K	1473K	1573K
$c_1$	0	2.62E-35	2.53E-31	9.28E-31	6.39E-30	3.24E-29	2.92E-28
$c_2$	0	3.431	3.391	3.399	3.392	3.39	3.398
$c_3$	0	-0.249	-0.475	-0.489	-0.512	-0.567	-0.589
$c_4$	0	0	0	0	0	0	0

An appropriate material model for a given material depends on both the chosen model equation and the associated dataset for that model's coefficients. In our work, we present optimized datasets for the 16MND5 material model, as displayed in Table 2.2 and Table 2.3,

respectively. These datasets are obtained using a particle swarm optimization algorithm implemented in MATLAB.

For an effective prediction of the RPVs behaviour during severe accidents, it is necessary to validate the selected material models. Here, the tensile-creep test [24] and RUPATHER Test #14 [31], are chosen for the validations. These validations involve a comparative study with creep models used in other literature [32 - 34], denoted by NB, CTH, and SH models in this study (see Table 2.4). The proposed dataset for the SH model in this thesis is denoted by the New-SH model.

Table 2.4. Creep models used in the comparative analysis.

NO.	Model	Dataset	Authors
NB model	Norton-Bailey creep law	[32]	Fischer, M. et al.
CTH model	Combined time hardening model	[33]	Villanueva, W. et al.
SH model	Strain hardening model	[34]	Ikonen, K.
New-SH model	Strain hardening model	-	-

The New-SH model shows a better agreement against two experimental results. Fig. 2.7 shows the validation results against the tensile-creep experiment. The numerical results of the optimal model (New-SH model) are observed to have relatively minor discrepancies when compared with the results obtained from experimental measurement for the strain evolution at different stresses. Further, the validation result against RUPATHER Test #14, as shown in Fig. 2.8 and Fig. 2.9, illustrates the better performance of the New-SH model from a macroscopic perspective. It better predicts the evolution and distribution of displacement of the tube in RUPATHER Test #14.

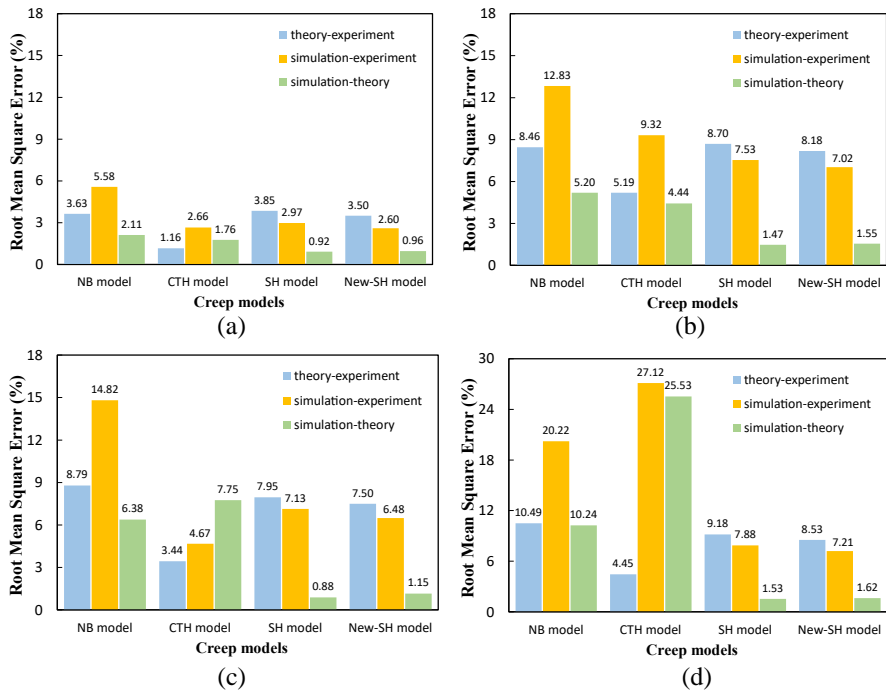


Figure 2.7. Samples of Root Mean Square Error (RMSE) of different creep models for 16MND5 at  $T = 1173$  K with stress of (a) 13 MPa, (b) 20 MPa, (c) 28 MPa, and (d) 38 MPa.

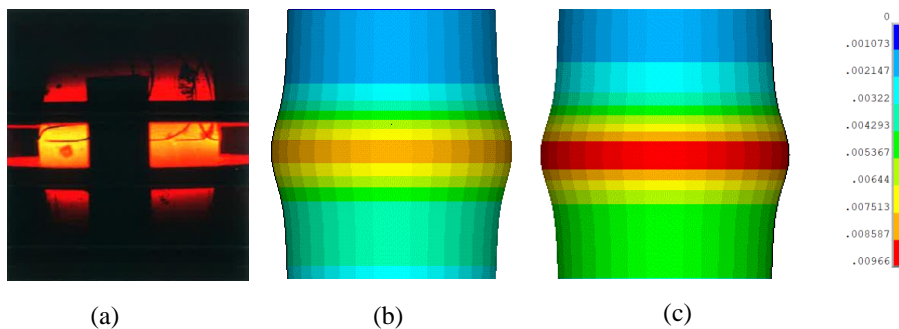


Figure 2.8. Tube deformation at 22083 s: (a) test piece photographed in the experiment [31]. (b) the numerical result with the SH model. (c) the numerical result with the New-SH model.

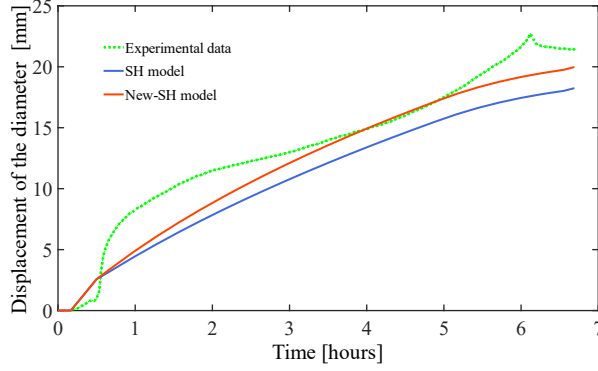


Figure 2.9. Comparison of simulated and experimental results for diameter evolution at the middle of the tube.

## 2.2.2 SA533B1 carbon steel

The material properties of carbon steel SA533B1, adopted from [15], have been used in establishing the material model of the RPV within a Nordic BWR in this study. The nonlinear isotropic (NISO) hardening model, detailed in Eq. (2.8), is also used here to describe the elastoplastic behaviour of SA533B1. The associated coefficients are listed in Table 2.5.

Table 2.5. Coefficients of NISO hardening model at different temperatures for SA533B1.

T	922K	1050K	1150K	1200K	1250K	1373K	1473K
$\sigma_0$	1.76E8	4.65E7	3.01E7	2.94E7	1.98E7	1.14E7	6.82E6
$R_0$	1.45E9	1.47E8	7.93E7	1.00E8	5.99E7	3.13E7	4.91E7
$R_\infty$	2.01E7	2.33E7	1.30E7	8.77E6	7.52E6	4.43E6	2.99E6
$b$	765.56	227.92	407.84	1545.6	89.93	83.30	174.45

In addition to the elastoplastic behaviour, the creep behaviour of this material is governed by a modified time hardening model as listed in Eq. (2.10). Its coefficients are presented in Table 2.6.

$$\varepsilon_{cr} = \frac{c_1 \sigma^{c_2} t^{c_3+1}}{c_3+1} \quad c_1 > 0 \quad (2.10)$$

where  $\varepsilon_{cr}$  is creep strain,  $t$  corresponds to the time in seconds at the end of sub-step,  $\delta$  is the stress in Pa, and  $c_i$  are constants.

Table 2.6. Coefficients of modified time hardening creep model at different temperatures for SA533B1.

T	643K	900K	1000K	1050K	1150K	1250K	1373K
$c_1$	0	6.35E-31	4.58E-41	9.07E-31	9.14E-41	4.54E-51	2.52E-48
$c_2$	0	2.947	4.2749	3.0602	4.7656	6.1262	5.7264
$c_3$	0	0.0733	0.7135	0.4897	-0.0427	0.4596	0.9001

Similarly, the validation of the material model of SA533B1 is first conducted against the uniaxial creep tests executed by the Idaho National Engineering Laboratory (INEL) [15]. The 2.29% strain of absolute difference and the 1.38% strain of RMSE illustrate a good agreement between the numerical and experimental results (see Fig. 2.10 (a)). In addition, the second validation is conducted against the creep tests carried out by CEA as part of the OLHF project [35]. The results, illustrated in Fig. 2.10 (b), indicate an absolute difference and RMSE not exceeding 2.2% and 1.68% strain, respectively.

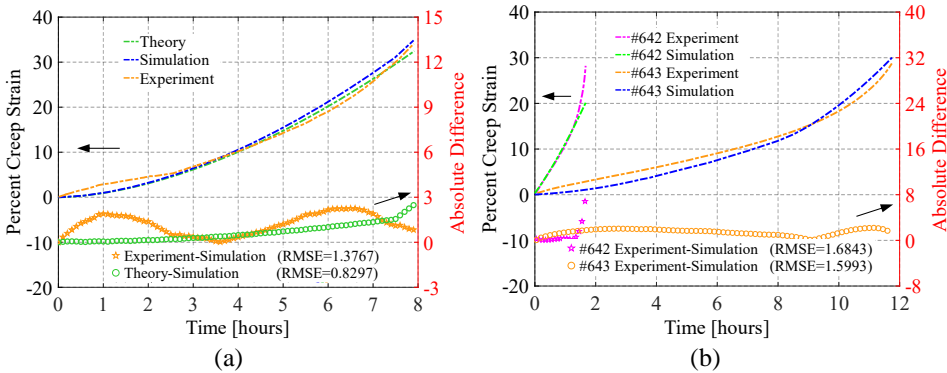


Figure 2.10. Validations of the material model against experiments: (a) a uniaxial creep test at  $T = 1000$  K with a stress of 39 MPa, and (b) creep tests on LHF at  $T = 994$  K with a stress of 73.6 MPa and  $T = 998$  K with 40.2 MPa.

The material models of 16MND5 and SA533B1, validated in this section, are employed in the thermo-mechanical analysis of RPV applications in Chapter 4 and Chapter 5.

### 2.3 Failure mechanisms

Four potential failure modes are generally identified in terms of RPV failure during severe accidents. These include lower head global rupture, melt impingement and melt-through, penetration tube heat-up and rupture, and penetration tube ejection [5, 14-16, 36-39].

However, given the diversity in NPPs design and the complexity of RPV behaviour during severe accidents, RPVs failure is not explicitly characterized for each failure mode.

In conducting numerical analysis on RPV failure during severe accidents, a common approach is to set up failure criteria based on the material properties, assessing components of the RPV structure (e.g., the vessel wall, the penetration tube, and the weld). This approach is feasible as these material properties can be characterized through tensile-creep tests, thereby providing the limits of the given material [35]. In the scope of this work, the melt-through, stress limit, and strain limit are adopted as failure criteria in implementing failure analysis of RPV applications, which are used in recent research (see Table 2.7).

Table 2.7. Examples of the literature for failure criteria used in structural analysis of RPV [3, 33, 34, 37, 40-44].

Authors/institutes	Objective	Platform /Approach	Failure Criteria
Mao et al., 2016/2017	AP600	ABAQUS	Strain & Stress-based
Koundy, et al. , 2005	Generic PWR	Analytical FE models	Strain & Stress-based
Kaneko, et al., 2015	low-alloy steel of RPV	Codes for Nuclear Power Generation	Stress-based
Villanueva et al., 2012	Nordic BWR	ANSYS APDL	Strain & Stress-based
Ikonen, 1998	RUPATHER# 14	PASULA	Strain & Stress-based
Peng Yu et al., 2019	FOREVER Tests	ANSYS_WORKBENCH	Strain-based
Sehgal et al., 2003	FOREVER Tests	ANSYS_APDL	Wall thickness change
VT., 2020	Benchmark on a PWR	ABAQUS	Strain & Stress-based
IBRAE., 2020	Benchmark on a PWR	HEFEST_M	Strain & Stress-based

### 2.3.1 Melt-through

During a severe accident, the inner surface temperature of the RPV increases continuously as a result of heating from the molten corium. This can induce local ablation of the wall if the temperature surpasses the material’s melting point. Afterwards, the molten corium is likely to fill in the ablated region, producing further ablation as the accident evolves. Consequently, the wall’s thickness progressively decreases, possibly leading to melt-through.

### 2.3.2 Stress failure

A stress-based failure criterion is frequently used in the engineering field. The stress limit of the given material is derived from experimental data in tensile tests. This ultimate stress is compared directly with the von Mises stress, which is obtained from the numerical analysis.

In the event that the von Mises stress in any region of the vessel surpasses this ultimate stress, it is inferred that material failure is imminent.

### **2.3.3 Strain failure**

Creep behaviour occurs at elevated temperatures, typically in the range of 0.3 to 0.4 times the melting temperatures for carbon steels [15, 19], even under moderate stresses that are below the stress limit. Therefore, the strain-based failure criteria become essential in predicting material failure within a thermo-mechanical analysis.

For RPV applications, 10% and 20% creep strains indicate the onset of the secondary and tertiary stages (as shown in Fig. 2.3) [23]. Afterwards, the tertiary stage tends to rupture rapidly, based partially on experimental creep data, we expect that failure is imminent once the creep strain reaches the threshold of 20%. Hence, a 20% creep strain is considered a strain-based failure criterion, while a total strain range of 25%-30% is also a consideration [15, 42].

In this study, RPV failure is deemed to have occurred if any of the following conditions is satisfied: (i) melt-through of the vessel wall occurs, (ii) the von Mises stress exceeds the ultimate stress, (iii) the creep strain exceeds 20%, or (iv) the total strain exceeds 25%.

## Chapter 3 Computational framework and tools

In this chapter, a methodology is proposed for the assessment of RPV structural behaviour during a severe accident. Firstly, the computational framework is discussed, followed by an introduction to the numerical tools. Then the proposed methodology is used in the thermo-mechanical assessment of RPV under different severe accident scenarios.

### 3.1 Computational framework

The development of the nuclear power safety requires an understanding of the accident sequence and the major physicochemical phenomena that can happen during the entire severe accident scenario. Given the complexity, cost, and safety considerations associated with performing prototypic experiments, the development of computational approaches in modelling and simulation of severe accidents is crucial in enhancing confidence in nuclear energy operation and safety.

Severe Accident (SA) integral codes, such as MELCOR [45], MAAP [46], ASTEC [47], and others, are widely used to simulate the comprehensive accident sequence of Nuclear Power Plants (NPPs) during postulated severe accidents. These integral codes are typically composed of various modules or sub-packages, each dedicated to model physical phenomena. Further, the integration of these modules or sub-packages facilitates the simulation of interactions between major phenomena during accident sequences. An example is the thermal-hydraulics modelling of the lower head of the RPV and its link with the thermo-mechanical behaviour of the RPV wall, predicting the potential failure time and location.

After the Fukushima accident, interest in reactor pressure vessel behaviour and its performance during severe accidents has gained more attention. A detailed analysis of RPV behaviour can offer insights into mitigation strategies and cleanup procedures in the event of a vessel breach and relocation of debris outside of the RPV. Given the thermal-mechanical input obtained from integral codes regarding the lower head of the RPV, a comprehensive structural assessment of the RPV can be achieved using mechanical codes, such as ANSYS-APDL, WORKBENCH, and ABAQUS. The structural analysis of the RPV encompasses the global deformation, stress-strain response of the vessel, and all transient structural responses, thereby forming the foundation for the prediction of RPV integrity. In addition, the inclusion of key lower head features such as vessel penetrations is more straightforward in these mechanical platforms than what the integral codes can support.

Hence, considering the strength of integral codes in modelling accident sequences and the proficiency of mechanical codes in simulating the structural behaviour, a combined approach using both types of codes is employed to study RPV behaviour. This study proposes a methodology that illustrates the thermo-mechanical analysis of RPV by coupling ANSYS-APDL with MELCOR. This methodology not only considers the availability of computational resources but also takes into account the latest developments in failure criteria for RPV failure assessment.

Fig. 3.1 illustrates the framework of the thermo-mechanical analysis of RPVs, including proposed methodology, sensitivity analysis, model validations, generation of boundary conditions, and failure criteria. The main path of the methodology is the implementation of structural analysis in ANSYS-APDL, taking into account the thermal and mechanical loads calculated using MELCOR. It should be noted that the failure modes in MELCOR need to be initially deactivated to obtain the thermo-mechanical loads over a long period for the structural analysis in ANSYS. Following this, the accident scenario, under the same conditions, should be re-simulated in MELCOR with the failure modes activated. This double-step process allows for the comparison of the predicted timing and location of RPV failure from these two codes. This comparison provides insights into the failure analysis of the vessel lower head using different platforms.

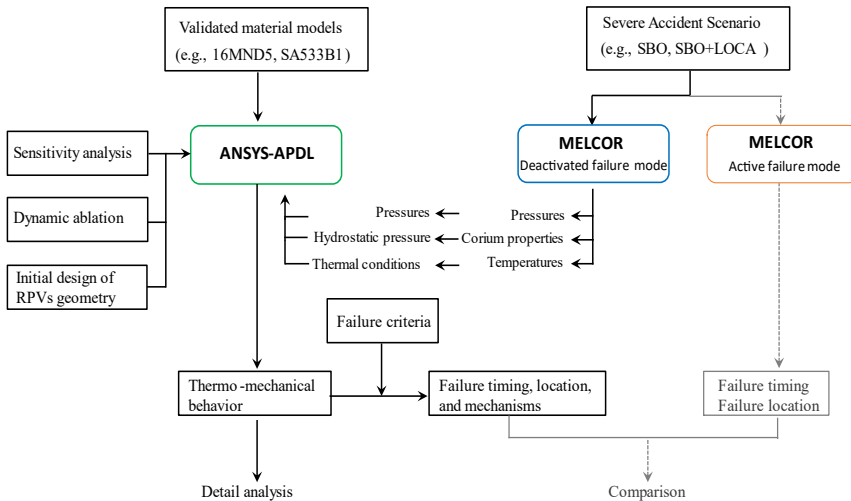


Figure 3.1. The framework of thermo-mechanical analysis of RPVs.

## 3.2 MELCOR

MELCOR is an integral code for the simulation of severe accidents in NPPs [48]. This code comprises a variety of models or sub-packages, such as the Core (COR) Package, Decay Heat (DCH) Package, and Cavity (CAV) Package, each addressing a specific phenomenon. Therefore, the holistic simulation of SA phenomena is achieved by interlinking these packages with parametric models that include core degradation, fission product release, hydrodynamics, and more.

The COR package models the behaviour of the core and lower plenum structure, adopting a two-dimensional geometry with radial rings and axial layers referred as COR nodalization. The results of the MELCOR simulation provide data that serves as the foundational input for subsequent Finite Element Analysis (FEA) software. These data include the vessel internal pressures, hydrostatic pressures due to the corium weight, and surface temperatures of the vessel wall and internal structures.

## 3.3 ANSYS Mechanical APDL

ANSYS Mechanical APDL, a popular tool within the FEA domain, is widely used in mechanical engineering analysis. This software enables users to perform nonlinear analyses using the Finite Element Method (FEM). FEM facilitates the division of a solid or structure into a finite number of elements connected via a set of nodes, wherein these elements share common edges with no overlapping. For mechanical problems, the displacement field  $\{\mathbf{u}\}$  of an element is firstly determined with nodal displacements and shape functions:

$$\{\mathbf{u}\} = \sum_{i=1}^{n_d} \{\mathbf{N}_i\} \{\mathbf{d}_i\} = \mathbf{N} \mathbf{d}_e \quad (3.1)$$

where  $n_d$  is the number of nodes forming the element,  $\mathbf{N}_i$  is the shape function for the  $i$ th node,  $\mathbf{d}_i$  is the nodal displacement at the  $i$ th node,  $\mathbf{d}_e$  is the displacement vector for the entire element, and  $\mathbf{N}$  is a matrix of shape functions for the nodes in this element. Note that the shape function is used to pre-define the shape of the displacement variations with respect to the node coordinates.

In a dynamic analysis, the purpose of FEM is to find an admissible displacement field  $\{\mathbf{u}\}$  which satisfies the energy principle:

$$\delta \int_{t_1}^{t_2} (\Pi - T - W_f) dt = 0 \quad (3.2)$$

$$\Pi = \frac{1}{2} \int_{V_e} \{\boldsymbol{\varepsilon}\}^T \{\boldsymbol{\sigma}\} dV \quad (3.3)$$

$$T = \frac{1}{2} \int_{V_e} \rho \{\dot{\mathbf{u}}\}^T \{\dot{\mathbf{u}}\} dV \quad (3.4)$$

$$W_f = \int_V \{\mathbf{u}\}^T \mathbf{f}_b dV + \int_S \{\mathbf{u}\}^T \mathbf{f}_s dS \quad (3.5)$$

where  $\Pi$  is the potential energy,  $T$  is the kinetic energy of the entire problem domain,  $W_f$  is the work done by the external force,  $V$  represents the whole volume of the solid,  $S$  represents the surface of the solid on which the surface forces are prescribed,  $\mathbf{f}_b$  is the vector of the body, and  $\mathbf{f}_s$  is the vector of surface force.  $\boldsymbol{\varepsilon}$  and  $\boldsymbol{\sigma}$  are the six tensors of strain and stress obtained using admissible displacement  $\{\mathbf{u}\}$  by:

$$\boldsymbol{\varepsilon} = \begin{bmatrix} \partial/\partial x & 0 & 0 \\ 0 & \partial/\partial y & 0 \\ 0 & 0 & \partial/\partial z \\ 0 & \partial/\partial z & \partial/\partial y \\ \partial/\partial z & 0 & \partial/\partial x \\ \partial/\partial y & \partial/\partial x & 0 \end{bmatrix} \mathbf{u} = \mathbf{L}\mathbf{u} \quad (3.6)$$

$$\boldsymbol{\sigma} = \mathbf{c}\boldsymbol{\varepsilon} \quad (3.7)$$

where  $\mathbf{c}$  is a matrix of material constants, in which Young's modulus  $E$ , Poisson's ratio  $\nu$ , and shear modulus  $G$ , respectively. They are usually obtained experimentally.

by substituting Eq. (3.1) and Eqs. (3.3) – (3.7) into Eq. (3.2), the energy principle can be expressed as

$$\delta \int_{t_1}^{t_2} \left\{ \frac{1}{2} \mathbf{d}_e^T \left( \int_{V_e} \{\mathbf{LN}\}^T \mathbf{c} \mathbf{LN} \mathbf{d}_e dV \right) \mathbf{d}_e - \frac{1}{2} \dot{\mathbf{d}}_e^T \left( \int_{V_e} \rho \mathbf{N}^T \mathbf{N} dV \right) \dot{\mathbf{d}}_e - \mathbf{d}_e^T \left( \int_{V_e} \mathbf{N}^T \mathbf{f}_b dV \right) - \mathbf{d}_e^T \left( \int_{S_e} \mathbf{N}^T \mathbf{f}_s dS \right) \right\} dt = 0 \quad (3.8)$$

by denoting

$$\mathbf{k}_e = \int_{V_e} \{\mathbf{LN}\}^T \mathbf{c} \mathbf{LN} \mathbf{d}_e dV \quad (3.9)$$

$$\mathbf{m}_e = \int_{V_e} \rho \mathbf{N}^T \mathbf{N} dV \quad (3.10)$$

$$\mathbf{f}_e = \mathbf{F}_b + \mathbf{F}_s = \int_{V_e} \mathbf{N}^T \mathbf{f}_b dV + \int_{S_e} \mathbf{N}^T \mathbf{f}_s dS \quad (3.11)$$

where  $\mathbf{k}_e$  is the element stiffness matrix,  $\mathbf{m}_e$  is the element mass matrix,  $\mathbf{F}_b$  and  $\mathbf{F}_s$  are the nodal forces equivalent to the body forces and surface forces applied on the element, which can be summarized as the total nodal force vector  $\mathbf{f}_e$ . The energy principle as in Eq. (3.8) can then be rewritten as

$$\delta \int_{t_1}^{t_2} \left( \frac{1}{2} \dot{\mathbf{d}}_e^T \mathbf{k}_e \mathbf{d}_e - \frac{1}{2} \dot{\mathbf{d}}_e^T \mathbf{m}_e \ddot{\mathbf{d}}_e - \dot{\mathbf{d}}_e^T \mathbf{f}_e \right) dt = 0 \quad (3.12)$$

by integrating and considering the arbitrary nature of the variation of the displacements, we have the FE equation in Eq. (3.13) for an element based on the local coordinate system:

$$\mathbf{k}_e \mathbf{d}_e + \mathbf{m}_e \ddot{\mathbf{d}}_e = \mathbf{f}_e \quad (3.13)$$

To recombine all the element equations into a global system calculation, the Eq. (3.13) for the individual element can be assembled together into the global FE system equation:

$$\mathbf{K} \mathbf{D} + \mathbf{M} \ddot{\mathbf{D}} = \mathbf{F} \quad (3.14)$$

in which  $\mathbf{K}$  and  $\mathbf{M}$  are the global stiffness and mass matrix,  $\mathbf{D}$  is the displacement vector at all nodes in the entire problem region, and  $\mathbf{F}$  is external force vector.

The damping effect can be considered in solving transient problems in the form:

$$\mathbf{K} \mathbf{D} + \mathbf{C} \dot{\mathbf{D}} + \mathbf{M} \ddot{\mathbf{D}} = \mathbf{F} \quad (3.15)$$

where  $\mathbf{C}$  is the damping matrix determined experimentally.

By solving the global FE equation as listed in Eq.(3.15), we can obtain the displacement field and then address the detailed constitutive behaviour (i.e., the stress and strain) for an object, for example, the RPV lower plenum in this study.

### 3.4 LS-DYNA

In Section 3.1, a framework for structural analysis has been established. This framework coupling ANSYS and MELCOR enables a comprehensive study of both macro and micro thermo-mechanical behaviour of RPVs, inclusive of deformation and stress-strain response. This section introduces a new approach for the simulation of RPV behaviour, utilizing LS-DYNA. Numerical studies are performed to explore the unique advantage of LS-DYNA in modelling RPVs structural behaviour.

LS-DYNA is used to address multi-physics problems, including solid mechanics, heat transfer, and fluid dynamics, either as separate phenomena or in a coupled manner. While this application can be extended to more complex phenomena, the major focus here is on the behaviour of an RPV under transient loading conditions with possible failure by rupture (as depicted in Fig. 3.2), deemed as one of the possible failure modes for an RPV. Unlike the previously mentioned platforms, lacking the capability and associated models to predict the

rupture explicitly, LS-DYNA is able to capture rupture behaviour and provide insights into RPV's rupture mode of failure.



Figure 3.2. Rupture phenomenon in FOREVER Test [24]

Simulating RPV failure using LS-DYNA is a new approach in the field of nuclear safety research. This is also a complex implementation due to the multitude challenges involved, including the time-dependent material model, creep model, transient boundary conditions, and computational efficiency.

As a first try at simulating RPV rupture in LS-DYNA, the below simulation aims to illustrate LS-DYNA's ability to simulate rupture phenomenon in RPVs applications. This simulation considers the time-dependent feature of material properties and boundary conditions, as summarized in Table 3.1. For the purpose of deriving results quickly during this trial and testing stage, aluminum is used in the proposed model as opposed to carbon steel. This is because aluminum, being softer than carbon steel, undergoes rupture in a much shorter timeframe.

Table 3.1. The main features and material properties in the LS-DYNA model.

Analysis type	Thermo-mechanical analysis & transient analysis
Geometry	A 3D geometry consists of a vertical part and a hemisphere
Boundary conditions	Temperature and pressure
Material mechanical properties	Density, Young's modulus, Plastic hardening modulus, Poisson's ratio
Material thermal properties	Thermal conductivity, Coefficient of thermal expansion, Specific heat, etc.
Failure criterion	Plastic failure strain.
Material type	Common Aluminum.

Fig. 3.3 (a) presents the distributions of the temperature and pressure in the proposed model. The temperature is applied uniformly across the entire geometry (indicated by the orange color), and the internal pressure is localized (indicated by the blue color). In addition, both of them are time-dependent, as shown in Fig. 3.3 (b).

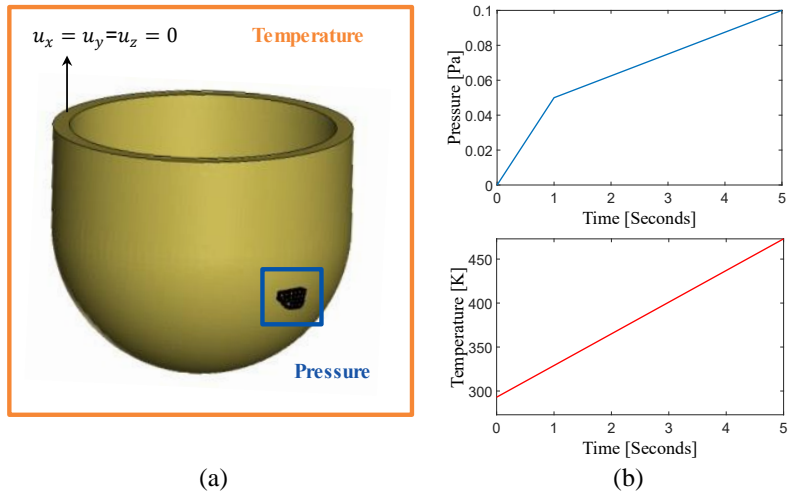


Figure 3.3. The geometry and boundary conditions of the proposed model in LS-DYNA.

The simulation results are shown in Fig. 3.4. Throughout the simulation period, the occurrence of rupture is observed predominantly in regions experiencing larger deformation and higher stress due to internal pressure. After this rupture, flying pieces are observed. Moreover, the displacement of these ejected pieces significantly accelerates at the moment of rupture (see Fig. 3.4 (d)). The understanding of the final breach can provide unprecedented insights onto the safety analysis of the RPV lower head during severe accidents. Despite the limitations and assumptions inherent to our current model, these findings demonstrate LS-DYNA's ability to simulate the RPV rupture phenomenon and to describe the thermo-mechanical behaviour of RPVs during severe accidents.

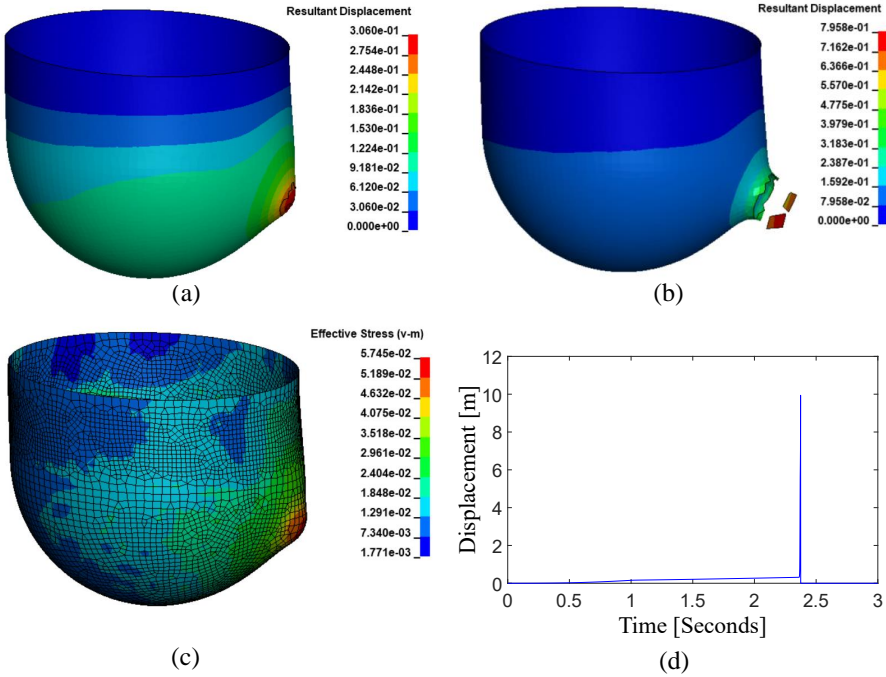


Figure 3.4. Examples of the simulation results of the proposed model in LS-DYNA: (a) Deformation at  $t = 2.2$  s, (b) Deformation at  $t = 2.36$  s, (c) Stress distribution at  $t = 2.35$  s, and (d) Nodal displacement of one fragment (1~3 s).

To further evaluate the capability of LS-DYNA in RPVs application, a more practical FEM model is established in LSDYNA, based on available experimental data from RUPATHER Test #14 (RT14) [31]. This model is dedicated to investigating the LSDYNA's capacity to simulate the structural behaviour of carbon steel 16MND5 under high temperature and continuous pressure. Table 3.2 shows three main parts of this LS-DYNA-based model. Furthermore, the parameters of the material model at varying temperatures are summarized in Table 3.3.

Table 3.2. An overview of the RT14 test model in LS-DYNA.

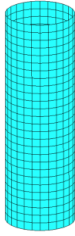
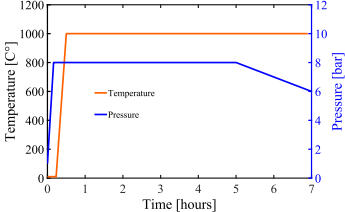
Part	FE model	Details
Geometry	<ul style="list-style-type: none"> <li>• Shell element</li> <li>• 2mm thickness</li> <li>• 27 vertical element number</li> <li>• 26 circumferential element number</li> </ul>	
Material model	<ul style="list-style-type: none"> <li>• 004-ELASTIC_PLASTIC_THERMA</li> <li>• T03-THERMAL_ISOTROPIC_TD</li> </ul>	
Boundary conditions	<ul style="list-style-type: none"> <li>• Time-dependent temperature</li> <li>• Time-dependent pressure</li> </ul>	

Table 3.3. Parameters of material model at different temperatures for 16MND5.

Temperature	293K	473K	673K	773K	873K	973K	1273K	1373K
Specific heat (mJ/ton K)	4.45E+08	5.19E+08	6.16E+08	6.96E+08	8.02E+08	1.16E+09	6.22E+08	6.26E+08
Thermal conductivity (mW/mm*K)	3.77E+01	4.03E+01	3.76E+01	3.54E+01	3.28E+01	2.85E+01	2.74E+01	2.84E+01
Young's modulus (Pa)	1.96E+05	1.99E+05	1.74E+05	1.61E+05	1.32E+05	4.78E+04	2.69E+04	2.50E+04
Poisson's ratio	3.00E-01	3.00E-01	3.00E-01	3.00E-01	3.00E-01	3.00E-01	3.00E-01	3.00E-01
Thermal expansion coefficients (m/m*K)	1.12E-05	1.25E-05	1.37E-05	1.43E-05	1.48E-05	1.52E-05	1.22E-05	1.32E-05
Density (ton/mm3)	7.85E-09	7.85E-09	7.85E-09	7.85E-09	7.85E-09	7.85E-09	7.85E-09	7.85E-09
yield stress $\sigma_0$ (MPa)	4.67E+02	4.00E+02	3.69E+02	3.59E+02	2.70E+02	1.11E+02	2.88E+01	1.38E+01
plastic hardening modulus $E_p$ (MPa/1)	1.71E+03	2.31E+03	2.25E+03	1.45E+03	4.77E+02	3.14E+02	4.05E+01	9.32E+01

Upon establishing the FE model of the RT14 test in LS-DYNA, the simulation is initially conducted for a real-time duration of 900 seconds due to the high computational cost. The results derived from the 900-second LS-DYNA simulation are displayed in Fig. 3.5 (a) and (b) and compared with corresponding results from the validated ANSYS-APDL simulation (refer to section 2.2.1). As can be observed, both temperature and displacement predicted by the LS-DYNA-based model agree favorably with those determined by the ANSYS-APDL simulation. Therefore, this LS-DYNA-based model is deemed capable of simulating the thermo-mechanical behaviour of the carbon steel 16MND5.

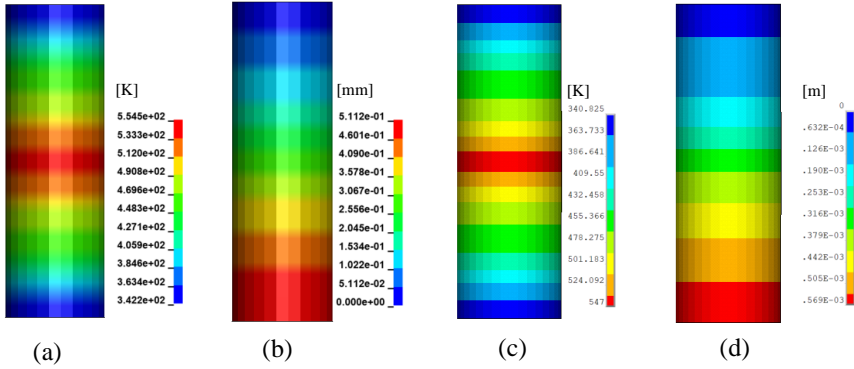


Figure 3.5. Comparison of the results: (a) temperature and (b) displacement distribution obtained from LS-DYNA, and (c) temperature and (d) displacement distribution obtained from ANSYS-APDL at  $t = 900$  s in the simulation of RUPTHER test #14.

Due to the high computational cost, the current computational device with 12 processors has difficulty simulating the entire duration of the RT14 test (i.e., more than 6 hours in real-time). As demonstrated in Fig. 3.6, a simulation for a real-time duration of 900 seconds in RT14 test consumes nearly 200 hours. Moreover, the correlation between computational time and real-time is not linear but more closely approximates an exponential increase. Therefore, an effective strategy to decrease the computational time is needed to enhance the usability of LS-DYNA in simulating the RT14 test, as well as the development of the LS-DYNA model in the simulation of RPVs application.

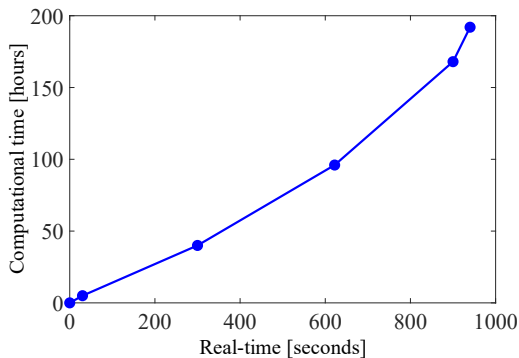


Figure3.6. The computational cost of the LS-DYNA model for RUPTHER test #14.

The computational time is strongly dependent on two factors: (i) computational efficiency and (ii) computational cost. The performance of the computational device, characterized by parameters such as the number of processors and the size of random-access memory (RAM), plays a crucial role in enhancing computational efficiency. Therefore, a computational device with higher performance is required for the LS-DYNA-based model's simulation, necessitating the use of High-Performance Computing (HPC). In addition, a way to reduce computational cost can be greatly beneficial, as discussed below.

In previous work, the models used in the ANSYS-APDL simulation of RT14, prior to the rupture, are validated. Although the rupture phenomenon cannot be simulated due to the limitation of the computational tool, the important thermo-mechanical behaviour can be reliably predicted. To proceed, instead of simulating the entire duration of the RT14 test using LS-DYNA (see Approach A in Fig. 3.7), a strategy of reducing computational cost is proposed (see Approach B in Fig. 3.7).

As illustrated in Approach B, the LS-DYNA can be used together with efficient FE model in APDL. That is, APDL is used for most of the simulation period, and the LS-DYNA simulation commences closer to the expected rupture time. The success of this approach heavily relies on the integration of the APDL results and the LS-DYNA FE model. Considering the formats of output files from APDL and input files for LS-DYNA, a workflow is presented in Fig. 3.8, outlining all necessary steps for the initialization and setup of the FE model in LS-DYNA.

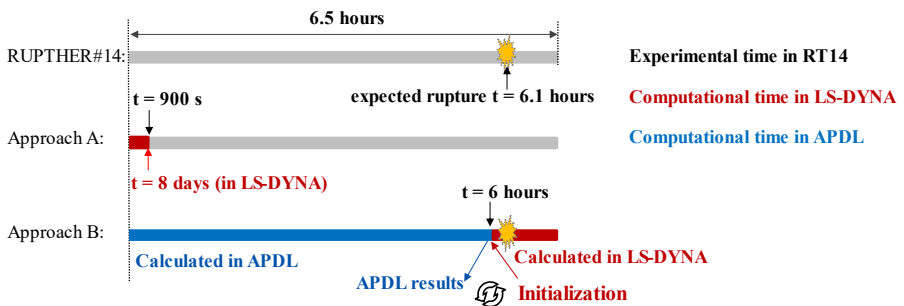


Figure 3.7. A proposed strategy to reduce the computational cost by combining the simulation of ANSYS-APDL and LS-DYNA.

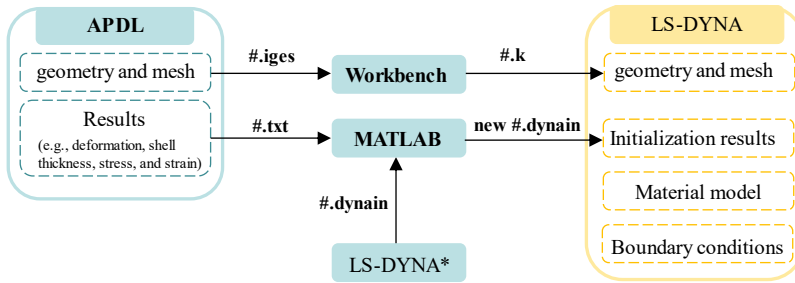


Figure 3.8. Working map of the initialization on LS-DYNA FE model with APDL results.

Initially, LS-DYNA reads the geometry and mesh from APDL (i.e., the #iges file), followed by the #dynain file. This #dynain contains keyword data for initializing deformation, shell thickness, and element history variables (stress and strain). Its initial format is generated by LS-DYNA and edited with APDL results using MATLAB. This procedure is still a work in progress, and results have not been obtained yet. However, the methodology is straightforward and can be useful in assessing RPV structural behaviour with the possibility of rupture.

## Chapter 4 Application to structural analysis in PWR design

In this chapter, the thermo-mechanical behaviour of RPVs in a generic PWR is investigated based on a common benchmark from the EU-IVMR project WP2.4 [49]. An overview of the benchmark problem is first provided, followed by a detailed process to develop the FE model. This chapter concludes with an exploration of the effect of the ablated profile on RPV failure within the numerical analysis, comparing the failure timing and internal pressure of ablated vessels characterized by a variety of fillet sizes. The content of this chapter is included in Paper 1.

### 4.1 Benchmark problem

In the event of a meltdown accident, the molten pool relocated in the lower head of the RPV stratifies into two-layer or three-layer, a consequence of the different densities within its complex composition. As illustrated in Fig. 4.1, the top layer is the metallic layer, generating a great deal of heat and therefore ablating the vessel's inner surface more seriously than other locations [50]. This phenomenon is known as the focusing effect. A common benchmark relevant to this phenomenon is introduced in the EU-IVMR project WP2.4 [49].

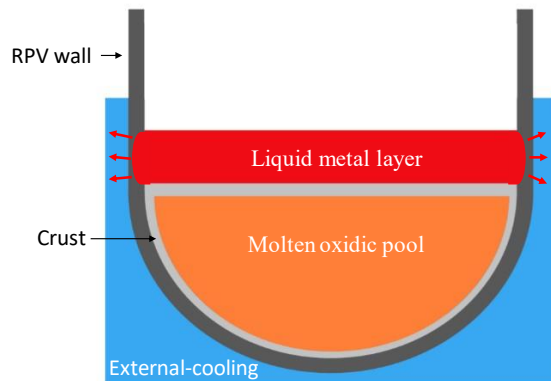


Figure 4.1. Schematic of a possible debris configuration in the RPV lower head during a severe accident with external vessel cooling.

The benchmark considers a generic PWR1000 design that includes specific details regarding RPV geometry, material properties, and boundary conditions. In this benchmark, the RPV is

simplified to a hemispherical lower head with a vertical cylinder, while the molten corium is assumed to display two-layered stratification (metal-over-oxide) with a critical heat flux of 2 MW/m<sup>2</sup> on the top layer. In addition, external vessel cooling is taken into consideration.

## 4.2 FE model

In accordance with the postulated accident scenario and the RPV characteristics outlined in the benchmark problem, a FE model of the RPV lower head has been established on the ANSYS-APDL platform, as shown in Fig. 4.2. The RPV profile is a 2D axisymmetric geometry with a severe ablation. This ablated region, being 0.4 m in height and 0.016 m in remaining thickness, is the result of the focusing effect. The constitutive model of the RPV material (specifically, 16MND5 carbon steel used in PWR design) is optional in the benchmark problem, and the validated model in Section 2.2.1 is used in the simulation below.

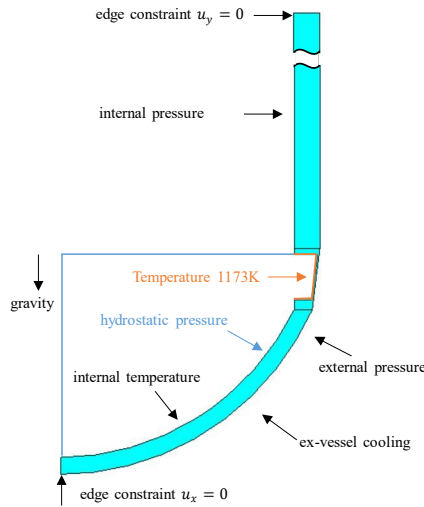


Figure 4.2. Schematic of the thermo-mechanical loads on the RPV lower head in the benchmark problem [49].

In addition to the general response of RPVs to thermo-mechanical conditions, this study places an emphasis on investigating the effect of the ablated profile on the numerical results. This is because of the simplification of the ablated corner as a rectangle, which could potentially lead to an excessive stress concentration and, subsequently, increase creep

damage. To reduce the effect of these artificial high stress and strain, a smoother edge for the ablated profile should be considered when conducting numerical analyses.

Firstly, three fillet radiuses with a slightly smoother edge for the ablated corners are introduced (i.e.,  $r = 1$  mm, 4 mm, and 12 mm as shown in Fig. 4.3 (b) – (d) ). Subsequently, two further fillet radiuses with a considerably smoother edge (i.e.,  $r = 80$  mm and 80\* mm as shown in Fig. 4.3 (e) – (f)) are considered. This consideration makes it closer to the realistically eroded state of an RPV resulting from the metal layer.

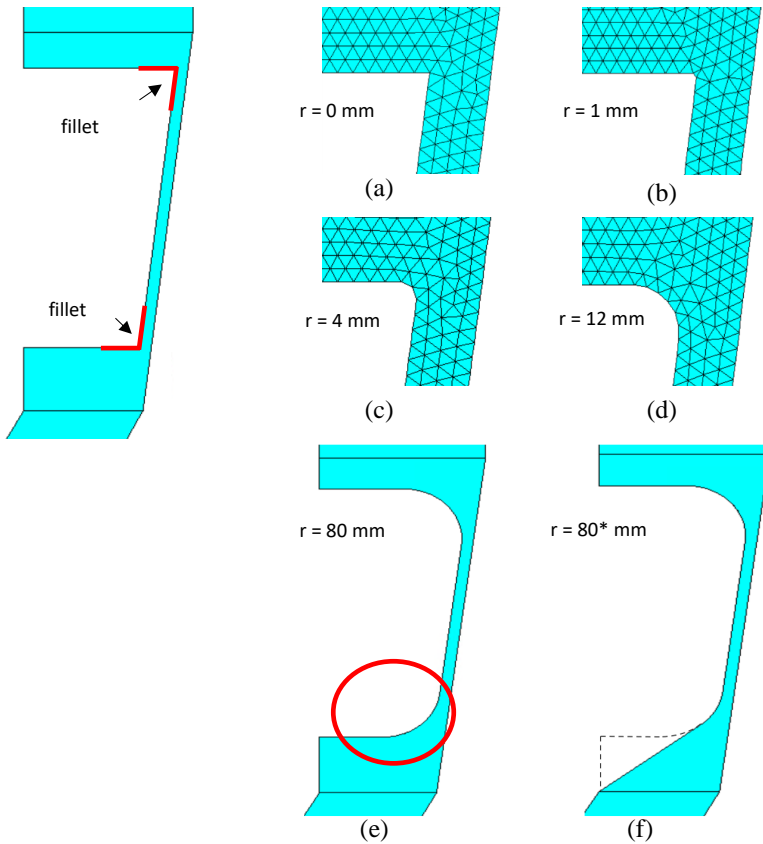


Figure 4.3. Detailed views of the RPV ablated wall with different sizes of fillets.

Meanwhile, the RPV behaviour under a series of internal pressures are compared. The lowest pressure with which the RPV will fail in a foreseeable period (72 hours) is called Failure Internal Pressure (FIP). Regarding the RPV failure criterion, the creep failure criterion (20%) is adopted, at which the time point is described as RPV Failure Time (FT) in the next section.

### 4.3 Results and discussion

Initially, the failure internal pressure (FIP) and failure time (FT) are investigated for slight fillet radiuses, including  $r = 0$  mm,  $r = 1$  mm,  $r = 4$  mm, and  $r = 12$  mm. As illustrated in Fig. 4.4, the RPV with a fillet of  $r = 0$  mm fails earlier ( $t = 3.6$  hours) under constant internal pressure (42 bars), in contrast to those with fillets of  $r = 1$  mm, 4 mm, and 12 mm, which fails at  $t = 4.1$  h, 5.5 h, and 10.5 h respectively (marked with blue). Moreover, this trend appears approximately linear. However, the FIPs are closely comparable across the fillet radius range of  $r = 0 \sim 12$  mm, only slightly increasing from 40.5 bars to 42 bars. In other words, the difference in FIP among the varying fillet radiuses is negligible, but the difference in FT is significant.

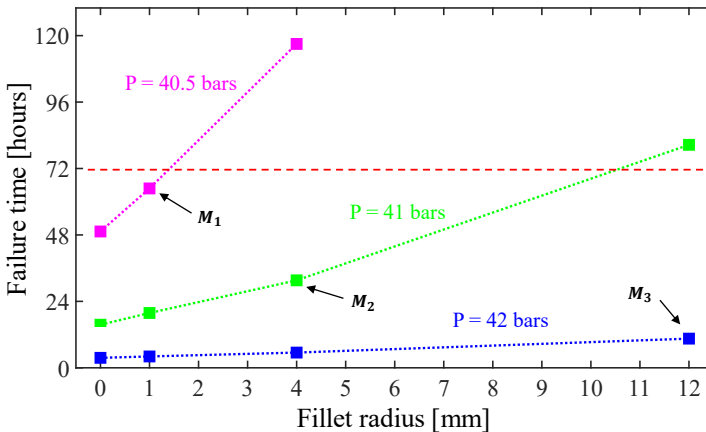


Figure 4.4. Correlation of failure time and fillet radius with various internal pressures.  $M_1$ ,  $M_2$ , and  $M_3$  indicate the failure internal pressure (FIP) of the RPV with fillet sizes  $r = 1$  mm,  $r = 4$  mm, and  $r = 12$  mm respectively.

When exploring the effects of further enlarging the fillet size from  $r = 12$  mm to  $r = 80$  mm and  $80$  mm\*, it is observed that the failure internal pressure increases to approximately 50 bars for both cases of  $r = 80$  mm and  $80$  mm\*, as shown in Fig. 4.5. However, the

difference in these FTs is more pronounced, with failure time of  $t = 31.4$  hours and  $t = 44.3$  hours respectively.

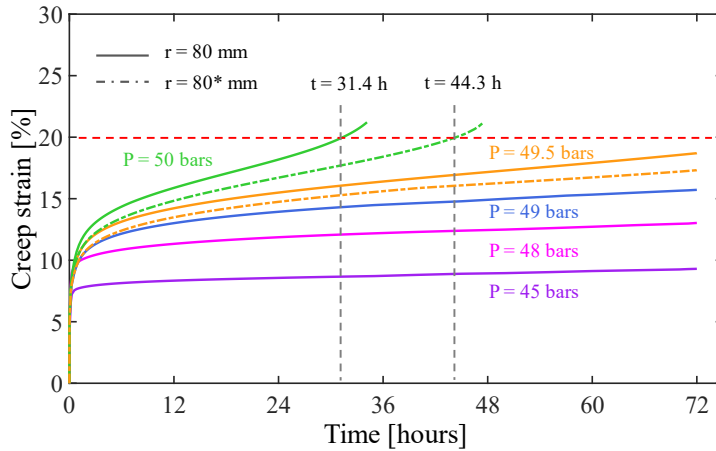


Figure 4.5. Correlation of maximum creep strain as function with time and internal pressure in the case of fillet size  $r = 80$  mm and  $r = 80^*$  mm

Generally, as the fillet size increases from  $r = 0$  mm to  $r = 80$  mm, the RPV tends to fail at an internal pressure of 40-50 bars within a confined time frame ( $t = 72$  hours). While the fillet radius demonstrates a negligible impact on the failure internal pressure, its influence on the failure time is markedly significant.



## **Chapter 5 Application to structural analysis in BWR design**

In this chapter, the model and methodology proposed in Chapter 2 and Chapter 3 are employed in the analysis of RPVs in a Nordic BWR. The structural analysis of RPVs with the IVR strategy is illustrated in Paper 2. Meanwhile, the failure analysis of RPVs is contained in Paper 3, and the analysis of penetration failure is detailed in Paper 4.

### **5.1 IVR feasibility**

During a meltdown accident, the core melts and relocates to the lower head of the RPV, and forms a debris bed which then heats up the inner surface of the vessel wall and threatens its structural integrity. One mitigation strategy for such severe accidents is In-vessel Melt Retention (IVR) [51]. The principle of this strategy is to retain the corium melts or the debris bed within the vessel lower head by using external cooling water, a method known as IVR-ERVC (external reactor vessel cooling). The success of IVR-ERVC hinges on the ability to transfer more heat from RPV to the cooling water than the critical heat fluxes (CHF) [52] at any location within the lower head of the RPV.

Analyzing RPV behaviour during different severe events is important for evaluating the feasibility of IVR-ERVC. This section explores the integrity of RPVs in a Nordic BWR under IVR-ERVC conditions during two severe accident scenarios: a Station Blackout (SBO) and an SBO combined with a Loss-of-coolant Accident (SBO+LOCA). The global deformation of the RPV lower head are initially presented. Subsequently, we demonstrate the stress-strain responses of the vessel wall and the safety margin under severe accidents with IVR based on the failure criteria.

#### **5.1.1 MELCOR model**

A Nordic BWR with an IVR-ERVC system is modelled in MELCOR, with the above-mentioned accident scenarios (i.e., SBO and SBO+LOCA ) [53, 54], as shown in Fig. 5.1. It also illustrates the hypothetical ERVC process through a flow path from CV410 to CV400. Nonetheless, it is important to note that this ERVC system, though assumed for this analysis, is not deployed in any actual Nordic BWR. Key parameters of the Nordic BWR design and the MELCOR setting are summarized in Table 5.1.

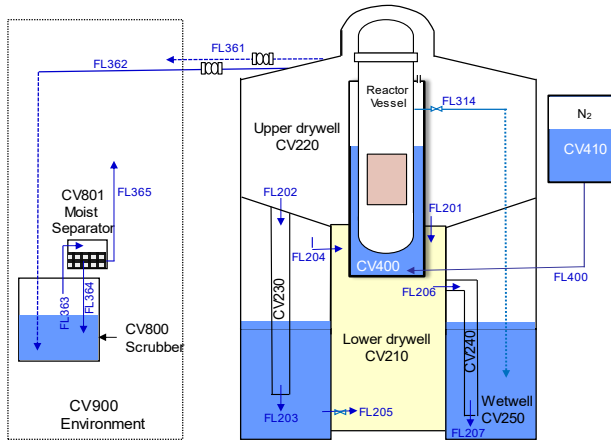


Figure 5.1. Schematic of the containment nodalization of a Nordic BWR with ERVC [53].

Table 5.1. Major parameters and settings of Nordic BWR design in MELCOR.

Parameters	Values	Setting in MELCOR	State
Nominal power	3000 MWth	Considered accident events	SBO/SBO+LOCA
Vessel lower plenum radius	3.2 m	Penetration model and failure	Off
Vessel lower plenum height	5.398 m	Automatic depressurization system	On
Vessel lower head thickness	0.198 m	Emergency core cooling system	Off
Break area in SBO+LOCA	0.1m <sup>2</sup>	IVR strategy	On

In the MELCOR simulation, three configurations of the COR package nodalization are considered for each postulated accident scenario (refer to Fig. 5.2), forming a calculation matrix listed in Table 5.2. In the scope of this work, we mainly focus on the RPV behaviour in structural analysis among the calculation matrix.

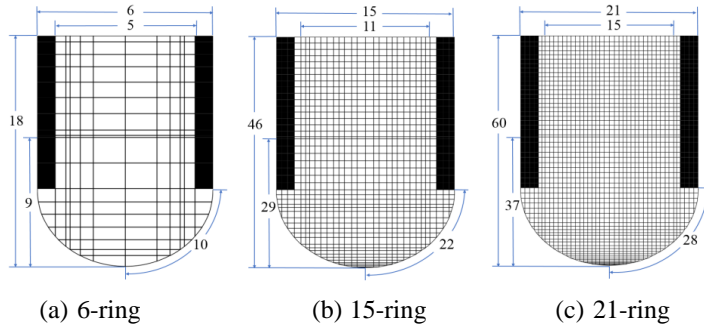


Figure 5.2. Coarse, medium, and fine nodalization in COR package of MELCOR simulation [53].

Table 5.2. Calculation matrix.

	Coarse mesh (6 rings)	Medium mesh (15 rings)	Fine mesh (21 rings)
SBO	SBO-6	SBO-15	SBO-21
SBO+LOCA	SBO+LOCA-6	SBO+LOCA-15	SBO+LOCA-21

### 5.1.2 FE model

The methodology outlined in Chapter 3 is used for structural analysis in this section. Each FE model in the calculation matrix (see Table 5.2) is established based on the corresponding output data from the MELCOR simulation. In addition, the material model of SA533B1 carbon steel, validated in Section 2.2.2, is integrated into each FE model. As an example, Fig. 5.3 shows the ablated geometry, loads, and constraints of the RPV for the SBO-15 case.

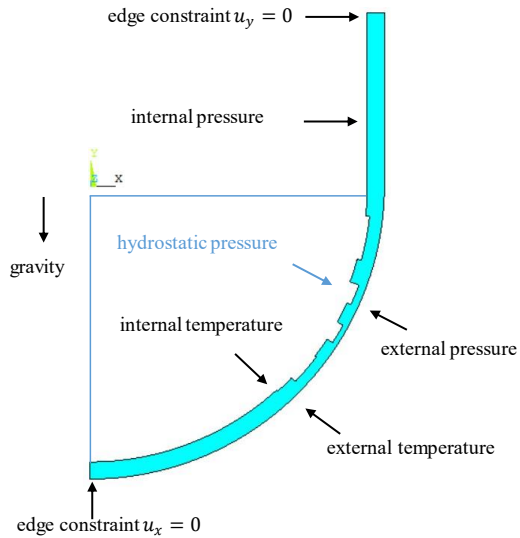


Figure 5.3. 2D axisymmetric geometry of ablated RPV, loads and constraints for SBO-15 case.

### 5.1.3 Results and discussion

Fig. 5.4 shows the global deformation of the vessel lower head at  $t = 12$  hours for the SBO+LOCA-21. The largest deformation, approximately 2.8 cm, is evidently located in the region with the greatest ablation. This is mainly due to the lateral displacement of about 2.1 cm (Fig. 5.4 (b) ). Additionally, significant deformation, around 2.4 cm, can be observed at the vessel bottom (Fig. 5.4 (a) ). This deformation is largely a downward shift due to the mechanical load. Similar results can be observed in the remaining five cases, though they are not shown here.

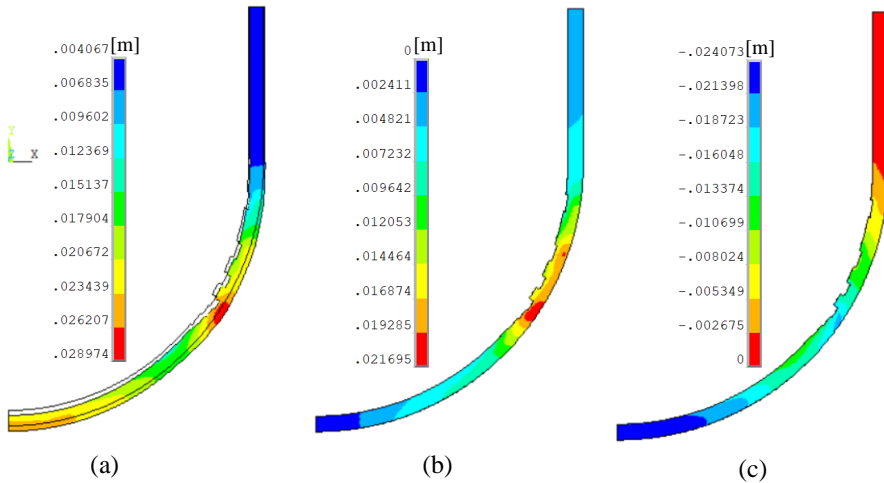


Figure 5.4. (a) Displacement vector sum, (b) x-component of displacement, and (c) y-component of displacement for SBO+LOCA-21 at time  $t = 12$  h.

We compare the ultimate stress of SA533B1 and the von Mises stress of the vessel at  $t = 12$  hours in each case. Notably, the ultimate stress is time-dependent [15]. In Fig. 5.5, the solid line represents the ultimate stress of the vessel material at different temperatures, while the dotted line represents the von Mises stress distributed within the vessel wall across various temperatures. It can be observed that, in all cases, the von Mises stresses consistently remain below the ultimate stress. Their smallest difference is at 10 MPa in the range over 1100 K, and in the range below 1100 K, the von Mises stress is at a minimum 58 MPa lower than the ultimate stress. This margin is considered sufficient, indicating that the structural integrity can be maintained when evaluated with the stress-based failure criterion.

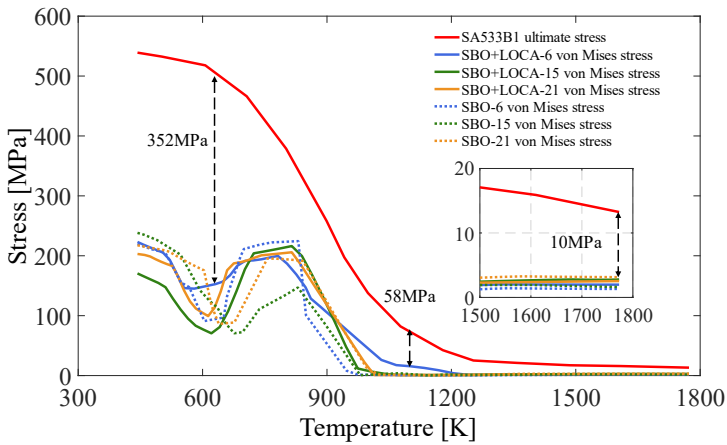


Figure 5.5. Comparison of von Mises stress and ultimate stress at  $t = 12$  h.

Fig. 5.6 illustrates a snapshot of the total strain of the vessel wall for the SBO+LOCA-21 case at  $t=12$  hours. The strain profile stabilizes after 6 hours, agreeing with the temperature history. The total strain observed in the inner region of the vessel wall is bigger than that in the outer region. This is attributed to the continuous heating of the vessel inner surface by the corium, while the outer region is subjected to direct cooling via the ex-vessel cooling process. In addition, the maximum total strain is located at the region with the largest ablation, which is induced by the high thermal loads in this region.

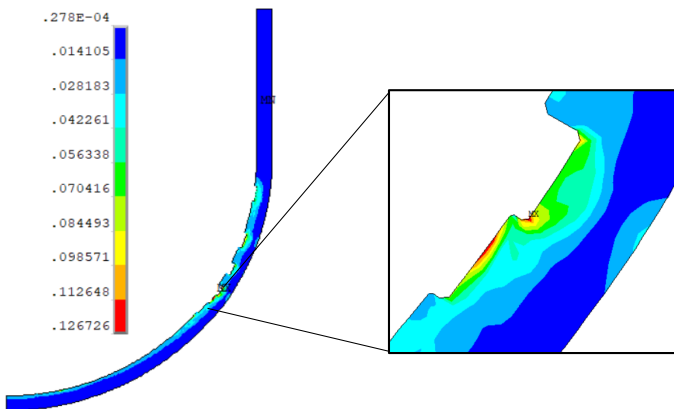


Figure 5.6. Total strain for SBO+LOCA-21 case at time  $t = 12$  h.

As mentioned in Section 2.1, total strain is the sum of creep strain  $\varepsilon_{creep}$ , plastic strain  $\varepsilon_{plastic}$ , and elastic strain  $\varepsilon_{elastic}$ . Fig. 5.7 shows the contributions of creep, plastic, and elastic strains to the maximum total strain at  $t = 12$  hours, with the height of bars indicating the strain values.

In all cases, creep strain (indicated in orange) is the primary contributor to total strain (indicated in grey), as compared to the elastoplastic strain (indicated in green and blue). Moreover, both the creep strains and total strains range from 7.8% to 13.1% and 9% to 14.4% respectively, which are sufficiently below the strain-based failure criteria set out in Section 2.3. Thus, these results indicate that the RPV can maintain its structural integrity based on the strain-based failure criteria.

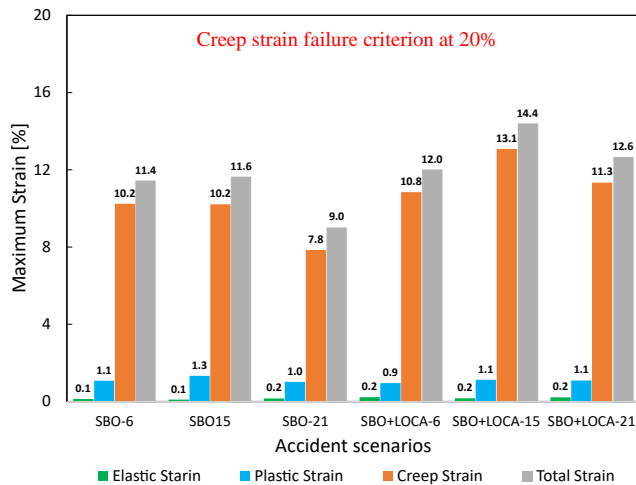


Figure 5.7. The magnitude of the strains at  $t = 12$  hours for 6 cases.

In this section, the RPV lower head can maintain its structural integrity under IVR in all cases considered. Following this, the behaviour of the RPVs under severe accident conditions without the IVR strategy is further investigated in Section 5.2.

## 5.2 RPV failure analysis

This section is mainly focused on evaluating RPV failure under postulated accident events: the SBO and SBO+LOCA.

### 5.2.1 MELCOR model

Fig. 5.8 shows the schematic of the MELCOR model adopted in this work, using the parameters and settings in Table 5.1, and it is noteworthy that the IVR-ERVC system is absent in this section. Both SBO and SBO+LOCA accident scenarios are simulated with fine mesh configuration for the COR package nodalization (Fig. 5.2 (c)).

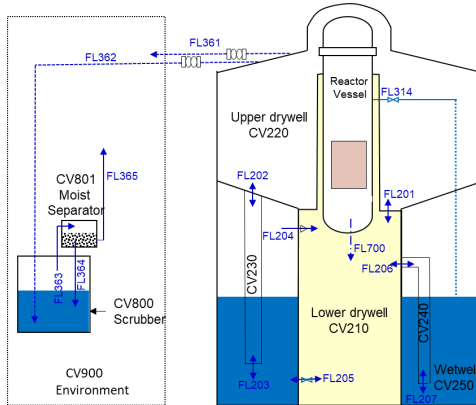


Figure 5.8. Schematic of the containment nodalization of a Nordic BWR [53].

### 5.2.2 FE model

In establishing the FE model, the material model and the methodology proposed in Section 2.2 and Section 3.1 have been employed. Compared to the constant ablated profile of the vessel lower head in structural analysis in Section 5.1, the vessel profile here is regularly updated in line with its ablation process, applying an ‘element killing’ approach. This approach can deactivate the elements with zero stiffness when their temperatures surpass the material’s melting temperature during the simulation. Consequently, the thermo-mechanical behaviour of the RPV lower head is investigated based on the dynamic profile of the vessel wall.

To accurately describe the detailed profile during the ablation process, a sufficiently fine mesh (comprising 40 layers of elements across the vessel wall) with an element length of 0.005 m is utilized, as shown in Fig. 5.9.

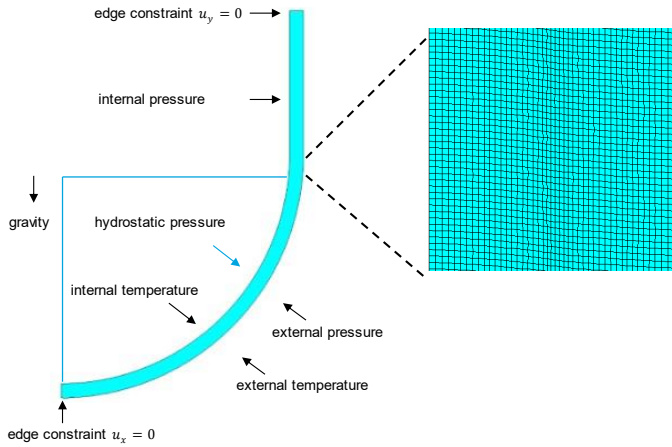


Figure 5.9. 2D axisymmetric geometry of ablated RPV, loads, constraints, and the mesh.

### 5.2.3 Results and discussion

Fig. 5.10 shows the critical snapshots of the RPV ablation process for the SBO scenario, as well as the corresponding temperature distribution at these moments. After about six hours, the vessel wall commences the ablation process, which intensifies over time, culminating in a melt-through after 7.22 hours. The melt-through region occurs at the upper surface of the RPV lower head ( $\theta = 62.5^\circ$ ), a region that consistently exhibits the thinnest cross-section of the vessel wall at any stage. A similar ablation process is observed in the SBO+LOCA scenario (not shown here), with the vessel commencing ablation and melt-through at around 6 h and 7.33 h, respectively. In this case, the melt-through region appears slightly lower, at  $\theta = 57.5^\circ$ .

The stress-strain behaviour of RPVs is transient and complex as the accident progresses. An initial examination of RPVs behaviour at  $t = 7.16$  h is conducted in the SBO case, as shown in Fig. 5.11. The results indicate that regions with severe ablations correspond to areas of higher temperature and larger creep strain. To investigate the failure time, location, and mechanism of the RPV, three critical locations are considered: (i) high-creep strain area (region A at angle  $46^\circ$ - $49^\circ$ ), (ii) high-ablation and high-temperature area (region B at angle  $60^\circ$ - $63^\circ$ ), and (iii) high-stress area (region C at angle  $83^\circ$ - $87^\circ$ ).

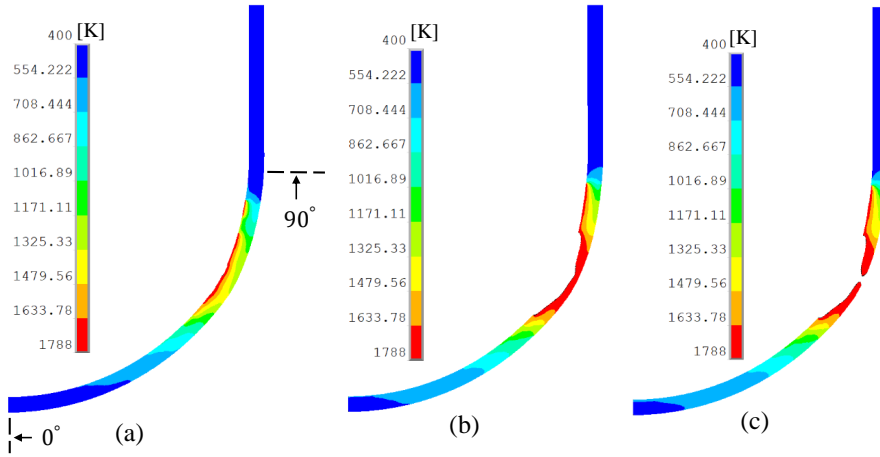


Figure 5.10. Dynamic ablation for SBO case: Temperature distribution [K] at time (a)  $t = 6$  h, (b)  $t = 7.16$  h, and (c)  $t = 7.22$  h.

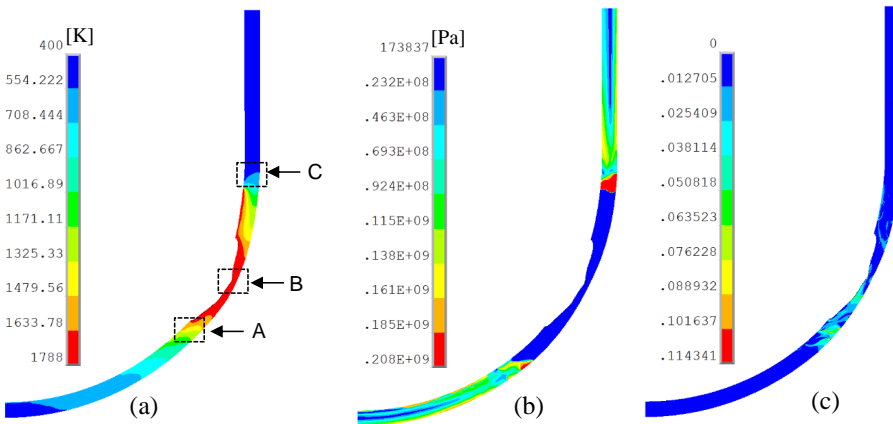


Figure 5.11. (a) Temperature distribution [K], (b) von Mises stress distribution [Pa], and (c) creep strain distribution of vessel wall at  $t = 7.16$  h for SBO case.

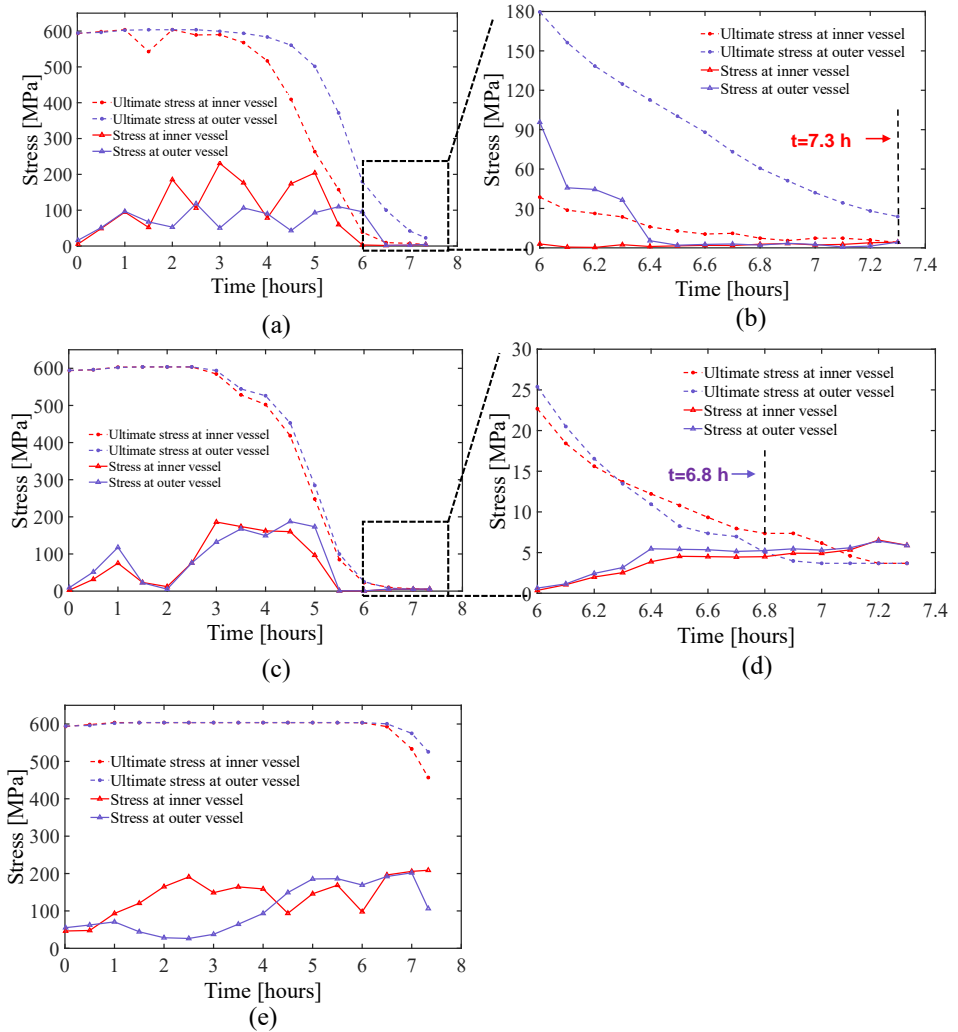


Figure 5.12. Comparison of von Mises stress of vessel and SA533B1 ultimate stress at the critical regions for SBO case (a) region A, (b) region A after 6 hours, (c) region B, (d) region B after 6 hours, and (e) region C.

As illustrated in Fig. 5.12, compared to regions A and C, the von Mises stress at the outer wall in region B is the first to exceed the ultimate stress of the steel at  $t = 6.8$  h. Furthermore,

to check if there is any strain failure preceding this stress failure, Fig. 5.13 presents creep and total strains at  $t = 6.8$  h. The results indicate that both the creep and total strains are well below the thresholds defined in the strain-based failure criteria, which are 20% for creep strain and 25% for total strain. Consequently, the RPV failure for the SBO case, which occurs at 6.8 h, is attributed to the stress failure mechanism. This occurrence precedes both a strain failure and a melt-through failure.

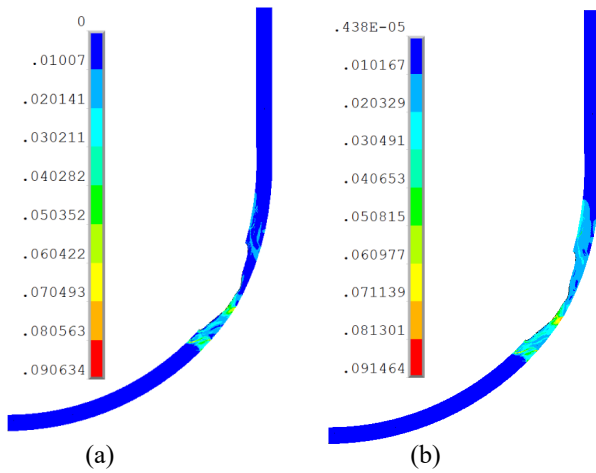


Figure 5.13. (a) creep strain, and (b) total strain of vessel wall at  $t = 6.8$  h for SBO case.

Similarly, a structural analysis of the RPV is also performed for the SBO+LOCA scenario. Table 5.3 summarizes the results of failure analysis using ANSYS-APDL, alongside relevant information on RPV failure from the MELCOR simulation. It is evident that the stress failure mechanism, rather than the strain failure and melt-through failure criteria, is the dominant failure mechanism in the structural analysis for both the SBO and SBO+LOCA scenarios. Moreover, the vessel fails at its thinnest regions in both accidents (i.e.,  $60^{\circ}$ - $63^{\circ}$  in the SBO case and  $55^{\circ}$ - $58^{\circ}$  in the SBO+LOCA case) at  $t = 6.8$  h and 7.1 h, respectively.

In comparison with the MELCOR failure information, the time and region of failure agree closely with the results obtained from ANSYS. Furthermore, the failure mechanism is also identified as stress-based, consistent with the findings from the structural analysis.

Table 5.3. The relevant information on RPV failure from ANSYS and MELCOR.

Accident scenarios	SBO case		SBO+LOCA case	
	ANSYS	MELCOR	ANSYS	MELCOR
Simulation tool	ANSYS	MELCOR	ANSYS	MELCOR
Failure time	t=6.8 hours	t=6.7 hours	t=7.1 hours	t=6.9 hours
Failure location	60°-63°	60.93°-63.89°	55°-58°	55.35°-57.88°
Failure mechanism	Breach of ultimate stress	Thru-wall yielding	Breach of ultimate stress	Thru-wall yielding

### 5.3 Penetration failure analysis

This chapter introduces a three-dimensional model for a vessel wall incorporating a cluster of IGT structures. Firstly, the behaviour of the welds within IGT structures is studied. Following this, the possibility of tube ejection failure is discussed.

Complementing the failure analysis of the RPV without penetration models in Section 5.2, this section aims to investigate the potential earliest failure mode of the RPV lower plenum, taking into account the ejection failure of the IGTs. Thus, the structural analysis conducted in this section utilizes the thermo-mechanical loads obtained from the MELCOR simulation for the SBO+LOCA case, outlined in Section 5.2.

Three representative locations of IGTs are considered as shown in Fig. 5.14: namely the bottom, middle, and farthest IGTs. The structure of each IGT is illustrated in Fig. 5.15, including a nozzle (marked in blue) and two weld joints (marked in purple). Notably, the penetration tube (marked in red) is not included in the FE model in this study. This simplification is made to especially focus on the weld failure, initiating the failure of the tube ejection.

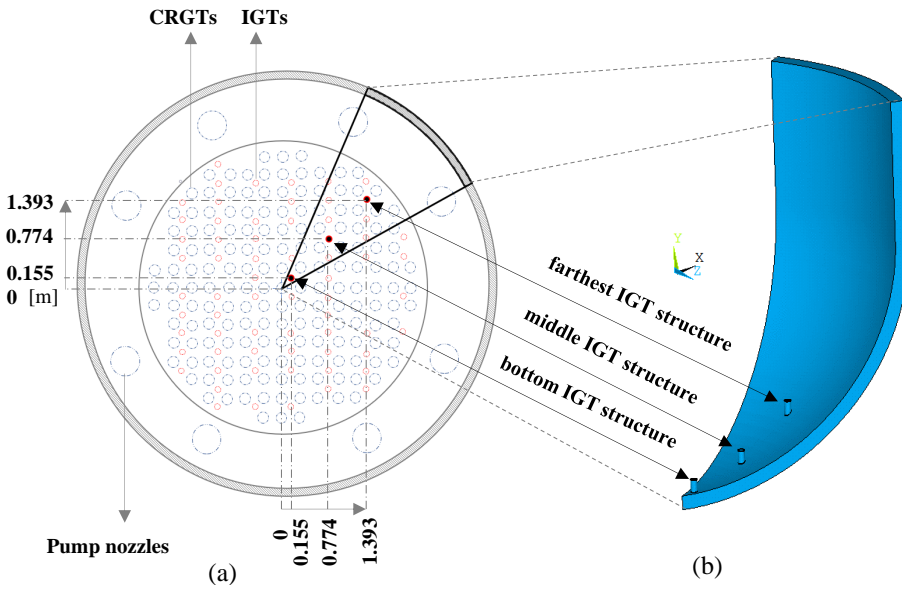


Figure 5.14. (a) Cross-section of BWR vessel lower plenum with CRGTs, IGTs, and pump nozzles, and (b) three-dimensional model of the RPV with a cluster of IGT structures.

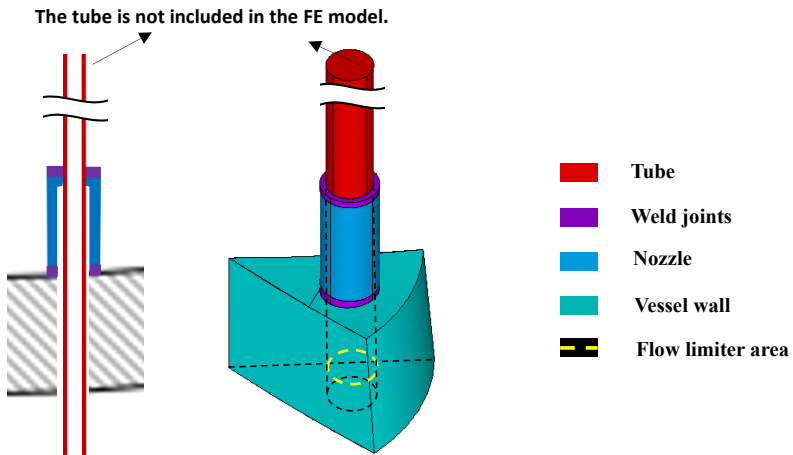


Figure 5.15. Example of 2D and 3D schematics for the Bottom IGT structure.

### 5.3.1 FE model

The FE model includes material models of SA533B1 carbon steel and Inconel-600 carbon steel. The proposed material model of the SA533B1 is employed for both the vessel wall and the nozzles [15]. For the weld joints, Inconel-600 is used [15], with the material model adopted from Ref. [38].

The boundary conditions for IGT structures in the structural analysis are obtained from the MELCOR simulation [53]. Given that the penetration model is not considered in the MELCOR simulation, conditions corresponding to the locations of the IGTs within the core region are extracted and subsequently used as boundary conditions for IGT structures in the ANSYS structural analysis. Fig. 5.16 shows the case of the bottom IGT structure, which is in the second ring within the core region and distributed axially from layer 1 to layer 7. Accordingly, this IGT structure encompasses seven cells, from which its thermo-mechanical loads are derived for the ANSYS structural analysis.

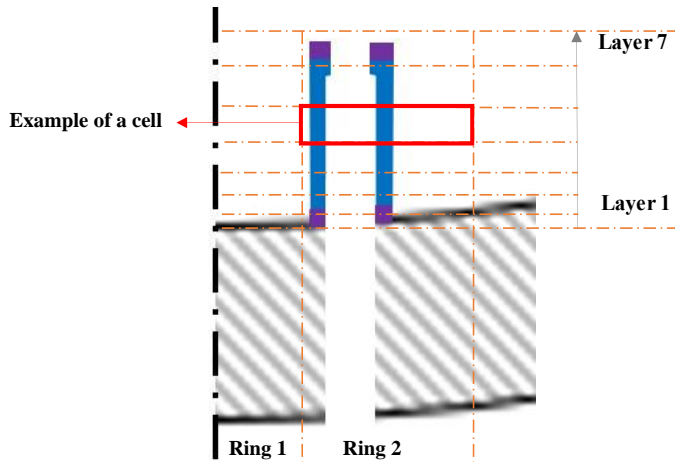


Figure 5.16. The scheme of core nodalization corresponding to the location of bottom IGT.

### 5.3.2 Results and discussion

Tube ejection is a significant failure mode of IGTs [15]. It is triggered by the failure of the top weld joint, which acts as the only support for the penetration tube. If the weld joint can no longer sustain the tube, the latter is forced outward under the vessel internal pressure,

leading to the release of molten material into the reactor cavity. Nevertheless, there exists a possibility to prevent the ejection of the tube by clamping it with the deformed vessel wall when the gap between them is reduced to 0 mm.

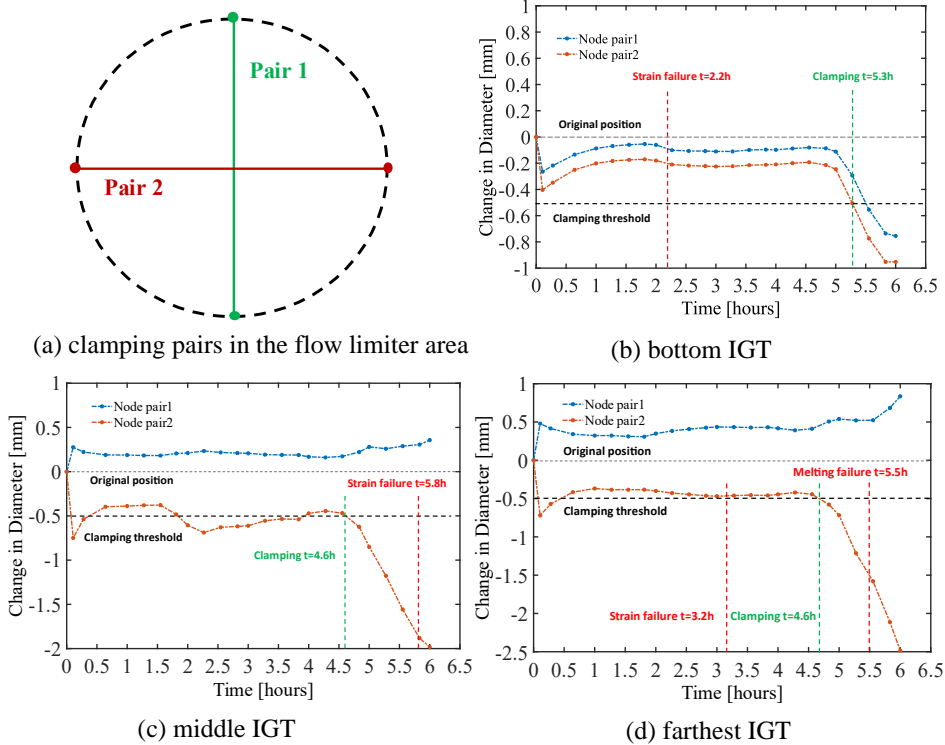


Figure 5.17. The changes in diameter of node pair 1 and 2 in the flow limiter area, in the bottom, middle, and farthest IGT structures.

The behaviour of the welds for all three IGT structures is first investigated with three failure criteria (i) melt-through, (ii) stress-based failure, and (iii) strain-based failure. As shown in Fig. 5.17, the top welds within the bottom and middle IGT structures undergo strain failure approximately at  $t = 2.2$  h and  $t = 5.8$  h, respectively. For the weld within the farthest IGT structure, apart from the strain failure at  $t = 3.2$  h, a melt-through failure is also found at  $t = 5.5$  h. However, none of the three IGT welds exhibits stress-based failure, as the von Mises stress for all three welds consistently remains well below their ultimate stress during the entire simulation.

While the welds fail to hold the penetration tubes in all three IGT structures during the SBO+LOCA scenario, the middle IGT exhibits early clamping at  $t = 4.6$  h, preventing ejection failure when the weld eventually fails at  $t = 5.8$  h. Conversely, for the bottom and farthest IGT structures, no clamping is observed before the weld failures, resulting in tube ejection failure once the welds give way. Additionally, the failure caused by these tube ejections occurs earlier than the vessel wall failure ( $t = 7.1$  hours) under the same accident scenario, illustrated in Table 5.3.



## Chapter 6 Conclusions and outlook

### 6.1 Conclusions

This thesis focuses on the formulation and development of FE model and method for assessing the RPVs performance during severe accident scenarios. Material models for two RPV structural materials are proposed and validated. The RPV lower plenum model is developed from a two-dimensional model for a standalone vessel wall to a three-dimensional model for a vessel wall with a cluster of IGT structures. A methodology is proposed to predict the thermo-mechanical behaviour of RPVs, estimate the mechanism and timing of RPV failure, and investigate the feasibility of IVR strategy mitigation during severe accidents. In addition, a preliminary model and promising method in LS-DYNA are introduced towards simulation of the possible rupture phenomenon of RPVs failure. The main contributions of this work are:

- A material model for 16MND5 carbon steel of RPVs relevant to a general PWR is established and validated. The study also examines the effect of fillet size on RPV failure analysis, in relation to both the failure internal pressure and the failure time. The simulation results indicate that, during the limited observation period ( $t = 72$  hours), the failure internal pressure remains within the range of 40-50 bars as the fillet radius increases from  $r = 0$  mm to  $r = 80$  mm. However, when discussing the effect of fillet size without considering the observation time limit, no significant difference in failure internal pressure is observed among the different fillet sizes. Instead, the fillet size has a considerable impact on the failure time. – **Paper 1**
- A material model for SA533B1 carbon steel of RPVs relevant to a Nordic BWR is established and validated. A one-way coupling approach between MELCOR and ANSYS is developed for assessing the structural behaviour of RPVs. The feasibility of the IVR strategy mitigation is explored during two severe accident scenarios, namely, SBO and SBO+LOCA. The simulation results show that the structural integrity of the RPVs can be maintained with the IVR strategy in these accident scenarios. Notably, the results highlight that the creep strain is the primary contributor to the total strain of the RPVs wall during the simulations. – **Paper 2**
- This study investigates the mechanism and timing of RPV failure in a Nordic BWR under severe accident scenarios. In addition, the dynamic ablation of the RPVs and

three failure criteria are considered. The simulation results show that RPV failure occurs at 6.8 hours in the SBO case and 7.1 hours in the SBO+LOCA case, with both failures attributed to the violation of the stress-based failure criterion. The weakest part of the vessel wall is located in a high-temperature region around  $\theta = 62.5^\circ$  from the bottom for the SBO case and  $\theta = 57.5^\circ$  for the SBO+LOCA case. – **Paper 3**

- The RPV lower plenum model is extended from a two-dimensional case for a standalone vessel wall to a three-dimensional configuration featuring a cluster of IGT structures. The performance of the welds during the SBO+LOCA scenario is studied. It is found that the strain failure occurs in all three top welds, while the melt-through failure is only observed in the weld of the farthest IGT structure. Furthermore, the analysis reveals that the ejection failure of middle IGT is prevented due to early clamping before weld failure. However, for the bottom and farthest IGTs, no clamping is observed prior to weld failure, leading to tube ejection failure upon the occurrence of weld failure. In addition, these tube ejection failures precede vessel wall failure in the considered SBO+LOCA scenario. – **Paper 4**

## 6.2 Outlook

- Further extension of the current material models for RPV structural materials, including the effect of ageing and radiation on the material properties, will be very meaningful.
- Investigation on how to improve the thermal boundary conditions for the structural analysis could contribute to the enhanced accuracy of RPVs behaviour predictions.
- The development of a global model, which includes an increased number of penetrations (e.g., Pump nozzles and CRGT structures) on the RPV lower head, alongside a comprehensive failure analysis, is worth studying.
- Enhancing the FE model for RPVs within LS-DYNA, along with the coupling model of heat transfer between the melt flow and the rupture wall, will be a possible research interest in the field of RPV safety analysis.

## References

1. A. Adamantiades, I. Kessides, Nuclear power for sustainable development: current status and future prospects, *Energy Policy*, 37 (2009) 5149-5166.
2. W.D. Magwood IV, L. Creswell, R. Gauntt, V.M. McCree, M. Weightman, N. Muroya, S. Morita, Y. Hah, X. Vasquez-Maignan, T. Ivanova, Fukushima Daiichi Nuclear Power Plant Accident, Ten Years On: Progress, Lessons and Challenges, Organisation for Economic Co-Operation and Development, (2021).
3. T. Kaneko, N. Tanaka, T. Yamaoka, H. Masaki, Y. Masuda, M. Iwanami, S. Ishioka, K. Fujii, Y. Goto, K. Saito, Evaluation of corrosion behaviours for reactor pressure vessels/primary containment vessels in Fukushima Daiichi units 1–3 nuclear power plant. *Journal of Nuclear Science and Technology*, 52 (2015) 773-783.
4. M. Pellegrini, K. Dolganov, L. Herranz, H. Bonneville, D. Luxat, M. Sonnenkalb, J. Ishikawa, J. Song, R. Gauntt, L.F. Moguel, Benchmark study of the accident at the Fukushima Daiichi NPS: best-estimate case comparison, *Nuclear Technology*, 196 (2016) 198-210.
5. M. Naitoh, M. Pellegrini, H. Mizouchi, H. Suzuki, H. Okada, Analysis of accident progression of Fukushima Daiichi NPPs with SAMPSON code, International Conference on Nuclear Engineering, American Society of Mechanical Engineers, (2013), pp. V006T015A023.
6. S. Sadek, S. Spalj, N. Debrecin, Analysis of SBO accident in NPP Krsko using RELAP5/SCDAPSIM/MOD3. 2, (2004).
7. M. Joyce, *Nuclear engineering: a conceptual introduction to nuclear power*, Butterworth-Heinemann, (2017).
8. R. O. A. Rahman and M. I. Ojovan, *Sustainability of Life Cycle Management for Nuclear Cementation-Based Technologies*, Woodhead Publishing, (2021).
9. R. Konings, T.R. Allen, R.E. Stoller, *Material properties/oxide fuels for light water reactors and fast neutron reactors*, (2012).
10. L.E. Weaver, *A Review of Accident Risks in Light-Water-Cooled Nuclear Power Plants*, *Nuclear Power Safety*, (1976) 303-349.

11. F.C. Rahim, M. Rahgoshay, S.K. Mousavian, A study of large break LOCA in the AP1000 reactor containment, *Progress in Nuclear Energy*, 54 (2012) 132-137.
12. Y.Y. Shen, H.W. Chou, C.C. Huang, R.F. Liu, Application of Probabilistic Fracture Mechanics Analysis on BWR Recirculation Piping Systems, *Pressure Vessels and Piping Conference*, American Society of Mechanical Engineers, (2016), pp. V06AT06A043.
13. H. Curet, S. Jensen, K. Richert, BWR and PWR LOCA methodologies, (2004).
14. H.G. Willschütz, E. Altstadt, B. Sehgal, F.-P. Weiss, Simulation of creep tests with French or German RPV-steel and investigation of a RPV-support against failure, *Annals of Nuclear Energy*, 30 (2003) 1033-1063.
15. J.L. Rempe, S.A. Chavez, and G.L. Thinnis, Light water reactor lower head failure analysis, Nuclear Regulatory Commission, Washington, DC (United States). Div. of Systems Research, (1993).
16. L.E. Herranz, J. Fontanet, E. Fernández, and C. López, Influence of the wet-well nodalization of a BWR3 Mark I on the containment thermal-hydraulic response during an SBO accident, *Nuclear Engineering and Design*, 295 (2015) 138-147.
17. D. Gandy, Carbon steel handbook, Electric Power Research Institute (EPRI), (2007).
18. G. Zagar, Deformation and Fracture Lab Course.
19. W.D. Callister and D.G. Rethwisch, *Materials science and engineering*. 5 (2011): John wiley & sons NY.
20. J. Mao, J. Zhu, S. Bao, L. Luo, Z. Gao, Creep deformation and damage behavior of reactor pressure vessel under core meltdown scenario, *International Journal of Pressure Vessels and Piping*, 139 (2016) 107-116.
21. M. E. Kassner, *Fundamentals of creep in metals and alloys*. Butterworth-Heinemann, (2015).
22. C. Öberg, *Creep Behaviour of High Temperature Cast Materials for Exhaust Applications*, KTH Royal Institute of Technology, (2020).
23. H.G. Willschütz, E. Altstadt, B. Sehgal, F.-P. Weiss, Coupled thermal structural analysis of LWR vessel creep failure experiments, *Nuclear Engineering and Design*, 208 (2001) 265-282.

24. C. Sainte Catherine, Tensile and creep tests material characterization of pressure vessel steel (16MND5) at high temperatures (20 up to 1300 C), European Commission Report INV-REVISA (98)-P008, (1998)
25. E.A. de Souza Neto, D. Peric, D.R. Owen, Computational methods for plasticity: theory and applications, John Wiley & Sons, (2011).
26. Z. Liu, X. Wang, R.E. Miller, J. Hu, X. Chen, Fracture toughness of thermal aged 16MND5 bainitic forging steel under varying 3D constraint conditions: An experimental study using SENT specimens, Theoretical and Applied Fracture Mechanics, 114 (2021) 103025.
27. T. Sharma, S.K. Bonagani, N.N. Kumar, D. Harish, K.M. Krishna, I. Samajdar, V. Kain, Effect of thermal aging on embrittlement of Cr–Mo–V pressure vessel steel, Journal of Nuclear Materials, 527 (2019) 151817.
28. R. Xing, D. Yu, G. Xie, Z. Yang, X. Wang, X. Chen, Effect of thermal aging on mechanical properties of a bainitic forging steel for reactor pressure vessel, Materials Science and Engineering: A, 720 (2018) 169-175.
29. V. Borodin, P. Vladimirov, Three-dimensional atomistic modelling of microcrack propagation in iron, Journal of nuclear materials, 416 (2011) 49-54.
30. M. Lambrecht, L. Malerba, A. Almazouzi, Influence of different chemical elements on irradiation-induced hardening embrittlement of RPV steels, Journal of Nuclear Materials, 378 (2008) 282-290.
31. P. Mongabure, M. Desmet, RUPATHER Test# 14-Rupture test at 1000 C and variable pressure 8 then 6 bars, Report SEMT/LISN/RT/99-003/A, CEA, France, (1999).
32. M. Fischer, A. Bernard, S. Bhandari, Post test analyses of Revisa benchmark based on a creep test at 1100 Celsius degrees performed on a notched tube, (2001).
33. W. Villanueva, A. Filippov, S. Jules, K. Lim, M. Jobst, A.M. Bouydo, S. Qais, H.D. Wang, F. Fichot, S. Bechta, Thermo-mechanical modelling of reactor pressure vessel during core melt in-vessel retention, Proc. of the International Seminar on In-vessel retention: outcomes of the IVMR project, Juan-les-Pins, France, (2020).
34. K. Ikonen, Revisa Rupther #14 Post-Test Analysis., VTT Energy, (1999).

35. L. Humphries, T. Chu, J. Bentz, R. Simpson, C. Hanks, W. Lu, B. Antoun, C. Robino, J. Puskar, P. Mongabure, OECD lower head failure project final report, Sandia National Laboratories, Albuquerque, NM, (2002) 87185-81139.
36. L. Li, M. Wang, W. Tian, G. Su, and S. Qiu, Severe accident analysis for a typical PWR using the MELCOR code, *Progress in Nuclear Energy*, 71 (2014) 30-38.
37. J. Mao, L. Hu, S. Bao, L. Luo, Z. Gao, Investigation on the RPV structural behaviors caused by various cooling water levels under severe accident, *Engineering Failure Analysis*, 79 (2017) 274-284.
38. Y. Yue, W. Villanueva, H. Wang, D. Wang, Thermo-mechanical analysis of instrumentation guide tube failure during a severe accident in a nordic boiling water reactor, *International Conference on Nuclear Engineering*, American Society of Mechanical Engineers, (2020), pp. V001T001A003.
39. D. Siegele, L. Hodulak, I. Varfolomeyev, and G. Nagel, Failure assessment of RPV nozzle under loss of coolant accident, *Nuclear engineering and design*, 193 (1999) 265-272.
40. V. Koundy, M. Durin, L. Nicolas, A. Combescure, Simplified modeling of a PWR reactor pressure vessel lower head failure in the case of a severe accident, *Nuclear Engineering and Design*, 235 (2005) 835-843.
41. J. Mao, J. Zhu, S. Bao, L. Luo, Z. Gao, Study on structural failure of RPV with geometric discontinuity under severe accident, *Nuclear Engineering and Design*, 307 (2016) 354-363.
42. W. Villanueva, C.-T. Tran, P. Kudinov, Coupled thermo-mechanical creep analysis for boiling water reactor pressure vessel lower head, *Nuclear Engineering and Design*, 249 (2012) 146-153.
43. P. Yu, W. Ma, W. Villanueva, A. Karbojian, S. Bechta, Validation of a thermo-fluid-structure coupling approach for RPV creep failure analysis against FOREVER-EC2 experiment, *Annals of Nuclear Energy*, 133 (2019) 637-648.
44. B. Sehgal, A. Theerthan, A. Giri, A. Karbojian, H. Willschütz, O. Kymäläinen, S. Vandroux, J. Bonnet, J. Seiler, K. Ikkonen, Assessment of reactor vessel integrity (ARVI), *Nuclear Engineering and Design*, 221 (2003) 23-53.

45. T.C. Wang, S.J. Wang, J.T. Teng, Comparison of severe accident results among SCDAP/RELAP5, MAAP, and MELCOR codes, *Nuclear technology*, 150 (2005) 145-152.
46. E. Beuzet, N. Bakouta, M. Boissavit, F. Haurais, A. Le Belguet, V. Lombard, M. Torkhani, Corium-related improvements in the EDF version of MAAP code in the frame of severe accident studies, *Proceedings of the 16th International Topical Meeting on Nuclear Reactor Thermal-Hydraulics, NURETH*, (2012).
47. L. Cantrel, F. Cousin, L. Bosland, K. Chevalier-Jabet, C. Marchetto, ASTEC V2 severe accident integral code: Fission product modelling and validation, *Nuclear Engineering and Design*, 272 (2014) 195-206.
48. L.L. Humphries, B.A. Beeny, F. Gelbard, D.L. Louie, and J. Phillips, *MELCOR Computer Code Manuals Vol.1: Primer and Users' Guide*, Albuquerque, NM 87185-0748, (2017).
49. W. Villanueva, S. Jules, A. Filippov, M. Jobst, Q. Saifi, K. Lim, and A. Bouydo, In-vessel melt retention severe accident management strategy for existing and future NPPs, *Mechanical Resistance of Reactor Pressure Vessel under In-Vessel Melt Retention Strategy, H2020 Programme*, (2020).
50. N. Chikhi, P. Fouquart, J. Delacroix, P. Piluso, Measurement of type 304L stainless steel and 16MND5 ferritic steel density and surface tension: possible impact for stratified molten pool, *Nuclear Technology*, 205 (2019) 200-212.
51. R.J. Park, K.H. Kang, S.W. Hong, H.Y. Kim, Detailed evaluation of melt pool configuration in the lower plenum of the APR1400 reactor vessel during severe accidents, *Annals of Nuclear Energy*, 75 (2015) 476-482.
52. R. Azizian, T. McKrell, K. Atkhen, J. Buongiorno, Effects of porous superhydrophilic surfaces on flow boiling critical heat flux in IVR accident scenarios, (2015).
53. Y. Chen, H. Zhang, W. Villanueva, W. Ma, S. Bechta, A sensitivity study of MELCOR nodalization for simulation of in-vessel severe accident progression in a boiling water reactor, *Nuclear Engineering and Design*, 343 (2019) 22-37.
54. Pershagen, *Light water reactor safety*, second, Pergamon Press, Oxford, (1996).

